8-31-2022

System Design for the Quantification of Microbial Motility in Extreme Environments

Megan Marie Dubay
Portland State University

Recommended Citation
Dubay, Megan Marie, "System Design for the Quantification of Microbial Motility in Extreme Environments" (2022). *Dissertations and Theses.* Paper 6184.
https://doi.org/10.15760/etd.8059

System Design for the Quantification of Microbial Motility in Extreme Environments

by

Megan Marie Dubay

A thesis submitted in partial fulfillment of the
requirements for the degree of

Master of Science
in
Physics

Thesis Committee:
Jay L. Nadeau, Chair
Drake Mitchell
Pui-tak Leung

Portland State University
2022

Abstract

Motility of microorganisms is understudied but provides useful insights into their behavior. Organisms' ability to move autonomously changes how they interact with their environment---finding nutrients, interacting with other organisms, and avoiding unfavorable conditions. Understanding motility features can also be used to identify specific species, such as the identification of *Vibrio cholerae* in human samples. Motility might also be used as evidence of life existing in even the most extreme environments on Earth, and possibly beyond. Specialized microscopy systems can be required to examine the motility of microorganisms due to the nature of the environments to which the instruments are exposed. For example, some extremophilic organisms cannot swim below 85°C, such as the thermophilic archaea *Pyrococcus furiosus*. To address these types of samples, we built a heated system for increasing ambient sample temperature up to 100°C with the ability to adjust and maintain such temperatures while performing microscopic imaging. This system has been used for the examination of the heat stress response of *Bacillus subtilis* and further work is being done to understand *P. furiosus*.

Another example of the need for specialized microscopy comes from the need for in situ observations. This includes Earth analog sites for the ocean worlds like Europa and Enceladus. These sites occur in environments where sample return is difficult and preservation of live organisms may be impossible. It also includes the restrictions and requirements for exposing these organisms to microgravity aboard the International

Space Station. Given increased virulence found in organisms in microgravity and the suppressed immune system of astronauts on board the International Space Station, special system considerations needed to be addressed for both astronaut safety and organism survival.

Dedication

This thesis is dedicated to the memory of my sister, Katy Lynn Dubay. She continues to be a constant reminder that life is too short to waste it on things that don't bring you happiness. Her enthusiasm for life encourages me to face things with optimism and passion.

It is also dedicated to the wonderful mentors I have had as I pursue my degrees. Namely: Kevin Dehne, Aurelian Balan, Norb Vance, and Dr. Aaron LaCluyzé. They saw the potential and enthusiasm in me, especially in times when I didn't see it myself. They saw an eagerness and love for this work and went above and beyond to encourage that. Their mentorship, advice, and support has been invaluable, and I would not have made it to this point without them.

Lastly, it is dedicated to my partner, Glennon Fagan. Thank you for the endless support and love. Thank you for keeping me going during all hard moments, burnout, and feelings that I wasn't adequate to be getting this degree.

Acknowledgements

First and foremost, thank you to my advisor—Dr. Jay Nadeau. This thesis would not have been possible without her. Thank you for taking me under your guidance at a time when I could not continue to afford to be here. Thank you for the support, wisdom, and mentorship. Jay is an unstoppable force in fighting to give graduate students the highest quality research, education, and opportunities. Her passion for improving physics education is an inspiration, and a mentality I will take with me throughout my career.

I am extremely grateful for my committee members: Dr. Drake Mitchell and Dr. Pui-tak Leung. I appreciate your mentoring, knowledge, expertise, and feedback. In addition, thank you to all the faculty members of the Portland State University Department of Physics. Thank you for providing the education and experience in getting this degree.

I would like to acknowledge the support of the National Science Foundation, the Jet Propulsion Laboratory, and the Center for the Advancement of Science in Space for funding the research described here.

Special thanks to Dr. Chris Lindensmith at Jet Propulsion Laboratory. Your guidance, knowledge, and experience have been invaluable. Thank you to the members of the Nadeau lab group, Charlotte Lipari, and Alex Smith. Your advice and encouragement are greatly appreciated. Lastly, thank you to the collaborators and project partners, without whom this work would not be possible.

Table of Contents

List of Tables

Chapter 2:

Chapter 3:

Chapter 4:

List of Figures

Chapter 2:

Chapter 3:

Chapter 4:

Glossary

DHM: Digital Holographic Microscope, described in detail later

FIJI : Fiji Is Just ImageJ, image processing and analysis software developed by NIH

JPL: Jet Propulsion Laboratory, California Institute of Technology

CASIS: Center for the Advancement of Science in Space

V. alginolyticus: the prokaryote *Vibrio alginolyticus*

B. subtilis: the prokaryote *Bacillus subtilis*

E. gracilis: eukaryotic organism *Euglena gracilis*

Sample chambers: part of a microscope system, in this case particularly for DHM, that contains the organism being studied. Typically consist of 2 optically-clear surfaces for imaging through and a middle well for the sample that is ~1mm thick.

HELM: Holographic Examination for Lifelike Motility, custom motility tracking software developed by a group at JPL

Bio-signature: evidence that something is living (ex: chemical analysis indicating active metabolism, biological analysis indicating proteins and amino acids found in living organisms)

Chapter 1: Introductory Chapter

The work described in this document covers three papers which are already published (Chapter 3) or in the process of submitting for publication (Chapters 2,4). Chapter 2, “A Literature Review of Methods for Analyzing Microbial Motility”, discusses common recent methods for quantifying motion of microbes. The focus of this review is specifically on methods for analyzing data obtained using Digital Holographic Microscopy (DHM), as this is the primary instrument type used for imaging in the work described. The instruments used in the work in Chapters 2,4 are off-axis DHMs and are described in greater detail in the published works.

Each portion of work in this document, as well as those that are not part of this, were done with the goal of understanding the motility of organisms in extreme environments. Microbes are found in all ecosystems on Earth, including marine and volcanic thermal vents and the veins of sea ice. The ability of organisms to survive in these conditions provides further confidence that life may have evolved elsewhere, even in our own solar system. Europa and Enceladus (moons of Jupiter and Saturn, respectively), have both been identified to have subsurface liquid water and are interests for life detection. Autonomous motion is known as a biosignature, a signature of living organisms, and could be used to detect life in the solar system.

To greater understand microbe responses to unfavorable environments, systems are being developed to simulate these environments, or even travel to these places for in situ observations. The work described in Chapter 3, “Quantification of Motility of Bacillus subtilis at temperatures up to 84C using a submersible volumetric microscope and automated tracking”, involves the development of a heated system to use DHM to study motility at temperatures up to 100ºC. To provide a proof of concept, and expand knowledge of stress responses of the well-studied *B. subtilis,* samples were examined from temperatures ranging from 28C to 84C.

Chapter 4 is a detailed study of optical substrates for imaging through using DHM. This work was done, in part, to aid in design of custom sample chambers for a DHM system that is being deployed for scientific missions aboard the ISS, thanks to CASIS. The goal of this system is to study the effects of microgravity on motility, since motility in micro-organisms are linked to its pathogenicity, and bacteria have shown increased pathogenicity as a result of micro-gravity. Studies of this type are important to understanding how to best provide care for astronauts, as they are considered immunocompromised and exposed to microbes that can cause illnesses. Due to the nature of the ISS and the importance of astronaut safety, NASA and the ISS National Laboratory have strict safety standards that must be abided by. There are also physical limitations to sending samples to the ISS. Together, the considerations necessarily led to an in-depth look at alternatives to standard glass microscope chambers. The work described was a crucial first step into an ongoing project.

Chapter 2: A Literature Review of Methods for Analyzing Microbial Motility

Note: This chapter is the review article “Recent advances in experimental design and data analysis to characterize prokaryotic motility” by Megan M. Dubay, Jackie Acres, Max Riekeles, and Jay Nadeau. It was written with the intent to be submitted for publication in *FEMS Microbiology Reviews*. At time of publication of this thesis, it will be submitted for publication and under review. This chapter is formatted in the way required by the target journal.

Citation: Dubay MM, Acres J, Riekeles M, Nadeau JL. “Recent advances in experimental design and data analysis to characterize prokaryotic motility.” In progress for submission to *FEMS Microbiology Reviews,* 2022.

One of the most challenging aspects of studying the motility behaviors of micro-organisms is the process of tracking their movement to quantify these behaviors. Multiple software options have been developed to autonomously track a large quantity of cells, but success of using these tools varies due to limits in system design. Several factors must be considered when designing these systems, and the choices and limitations can impact the ability to quantify motility without extensive, tedious human intervention. We aim to discuss these options and limitations in this review as it guides the principles of system design discussed later.

Author Contributions: This was a collaborative effort of literature searches, discussion of material, writing, organization, and revisions.

Recent advances in experimental design and data analysis to characterize prokaryotic motility

Dubay, M. M., Acres, J., Riekeles, M. and Nadeau, J.L.

In process of final review before submission for publication.

Abstract

Bacterial motility plays a key role in important cell processes such as chemotaxis and biofilm formation, but is challenging to quantify due to the small size of the individual organisms and the complex interplay of biological and physical factors that influence motility phenotypes. Swimming, the first type of motility described in bacteria, still remains largely unquantified. Light microscopy has enabled qualitative characterization of swimming patterns seen in different strains, such as run and tumble, run-reverse-flick, run and slow, stop and coil, and push and pull. However, quantifying these behaviors (e.g., identifying run distances and speeds, turn angles and behavior by surfaces or cell-cell interactions) remains a challenging task. A qualitative and quantitative understanding of bacterial motility is needed to bridge the gap between experimentation, omics analysis, and bacterial motility theory. In this review, we discuss the strengths and limitations of how phase contrast microscopy, fluorescence microscopy, and digital holographic microscopy have been used to quantify bacterial motility. Approaches to automated software analysis, including cell recognition, tracking, and track analysis, are also discussed with a view to providing a guide for experimenters.

1.0 Introduction

Since the development of a tracking microscope in 1971[1], researchers have recognized the need for tools that would allow for both imaging and recording of microbial motility. The ideal experimental apparatus would record images of cells in a 3D volume with high signal to noise ratios and at high framerates. This would in turn allow cell tracking algorithms to easily characterize cell motility quickly and effectively, preferably with minimal user input. Advances over the past few decades have brought this ideal case closer to reality. Unfortunately, despite numerous experimental setups and data analysis techniques, the holy grail of precise and straightforward 3D tracking of bacteria remains elusive. That being said, progress has been made in understanding motility phenotypes of various bacteria which we will summarize here.

1.1 Bacterial motility

Motility is a crucial microbial phenotype that has evolved independently in Bacteria, Eukarya, and Archaea. On the molecular level, 18 different motility types can currently be identified, with more undoubtedly to be discovered in organisms that have not yet been cultured[2]. Some bacteria use flagella for swimming motility, whereas archaea use the unrelated archaellum[3,4]. Directional motion allows organisms to find nutrients, escape predators, waste products, and toxins, and assemble into biofilms. The best studied organisms are Escherichia coli and Salmonella enterica serovar Typhimurium, and much of what we know about motility and chemotaxis come from these organisms[5].

Research into different organisms with different motility patterns has grown over the past two decades, identifying new classes of motility, motility in new classes of organisms, and elucidating the physics of swimming at the micron scale. Flagellins are highly conserved in Bacteria, but flagellar conformations of bacteria and archaea vary greatly, as do body shapes (Fig. 1 a, b). At least six types of swimming patterns can be distinguished in low-resolution microscopic recordings; these correspond to both flagellar arrangement and function. The common gut and soil bacteria Escherichia coli and Bacillus subtilis have peritrichous flagella and show a well-characterized pattern of motility involving “runs” (where all the flagella rotate together in a bundle, turning counter-clockwise) and “tumbles” (where the flagella turn clockwise and the bundle separates) (Fig. 1 c). Bacteria with peritrichous flagella that only rotate clockwise can show run-and-stop or run-and-slow patterns [6] (Fig. 1 d). Another pattern, the “run-reverse flick” pattern of aquatic organisms with a single polar flagellum, such as Vibrio, is also known (Fig. 1 e) [7]. This pattern of swimming, common in marine bacteria, involves 180-degree reversals, creating zig-zag tracks, often at high speeds compared to bacteria with peritrichous flagella (up to 100 µm/s vs. 10-30 µm/s). Another type of swimming seen with a single flagellum is the stop-and-coil motion of organisms such as Rhodobacter sphaeroides, where the flagellum cannot reverse direction, so it coils in order to allow the organism to change orientation [8] (Fig. 1 f). Motile magnetotactic cocci have been identified that have peritrichous flagella and swim in a helical motion due to push-pull action of the flagella [9] (Fig. 1 g). Swimming patterns of spiral-shaped cells are characterized more by the appearance of the cells themselves rather than the track of movement. In Spirochetes such as Borrelia and Treponema, pairs of flagella rotate within the periplasm, generating a helical wave [10]. In spirochaetes, two "run" modes and two non-translational modes have been identified. In general, changes in flagellar number, arrangement, hook length, or other parameters profoundly affect motility and chemotaxis patterns [11].

Other types of swimming continue to be elucidated. Synechococcus is a cyanobacterium that swims without flagella[12]. Other types of non-swimming motility are also seen but are less understood. Type IV pili are used by many species for motility on surfaces, usually called twitching motility [13]. Gliding refers to a surface mechanism used by a heterogeneous group of bacteria, powered by ion channels and secretory mechanisms independent of flagella[14]. Sliding is a type of surface motility that requires no active motor [15]. Staphylococci, previously considered non-motile, have been shown to have means of locomotion that include spreading, darting, and comet formation [16]. In this review we focus on motility that is tracked in liquid medium, thus restricting our discussion to swimming and to some extent gliding.

Much less is known about swimming in Archaea, although it has been known for some time that swimming is induced by rotation of the archaellum. Much of the difficulty in studying these organisms arises from the need to observe them under extremophilic conditions: anaerobic, temperature extremes, and/or very high salt. A systematic study of the swimming patterns of several types of archaea was performed in 2012[17]. Some archaea show the fastest movement relative to body size of any known organism on Earth. The patterns of fast-swimming archaea were characterized as "run and seek," with different behaviors (slower zig-zagging) near the surface of the slide. The tracks are closest to the bacterial "run and flick" pattern, but many archaea are distinguished by their remarkable speeds.

High-resolution recordings permit observation of detailed features of tracks rather than characterizing all forward motion as simply "runs." These studies have led to an increasing appreciation of the importance of cell body shape in swimming. The cell body is often considered to be a source of passive drag, but non-rod-shaped cell bodies may contribute to motility. Many marine motile bacteria are curved rods falling within a relatively narrow range of elongation and curvature. Detailed models of swimming speeds and chemotaxis efficiencies have identified shapes that are optimized across a panel of selective parameters[18]. Even more recently, helical motion of a crescent-scaped bacterial cell, Caulobacter crescentus, was observed to affect swimming patterns in this singly flagellated cell[19].

Even greater increases in resolution permit single-molecule investigations of bacterial cells. These have been well reviewed elsewhere [20] and will not be considered in this review.

1.2 Imaging challenges

Understanding motility phenotypes provides a framework of what quantities might be of interest to characterize and quantify bacterial motility. For instance, the length of a bacterium's "run" could change based on environmental factors. Rapid characterization of run length for numerous cells would give good statistics and provide a sound basis of comparison. However, quantification of bacterial motility remains challenging due to the technological difficulty of imaging live, active organisms on the order of the size of 2λ of visible light that can move tens or even hundreds of cell lengths per second. For any imaging system, a variety of trade-offs must be made according to the specific goals of the experiment. Increased spatial resolution usually leads to decreased field of view, unless cameras with very high sensor sizes are used. High frame rates are necessary to capture fast processes but lead to extremely large datasets if carried out over long times. Fluorescent labels increase signal to noise of imaging, but dyes may affect microorganism behavior. Finally, data may be analyzed cell by cell, which optimizes accuracy but limits the number of cells considered; or statistical analyses may treat hundreds to thousands of cells at a time but fall prey to false positive and false negative identification of tracks.

The purpose of this review is to identify the recent breakthroughs in bacterial motility analysis and identify what parameters of an imaging system are necessary to study the identified phenomena and what the limiting technological factors are in each case. A summary is provided that should assist researchers in choosing imaging and tracking techniques that are appropriate for the systems studied, or in developing custom systems that can push the limits of what is currently known. Both hardware and software are considered, with particular attention to automated identification and tracking algorithms.

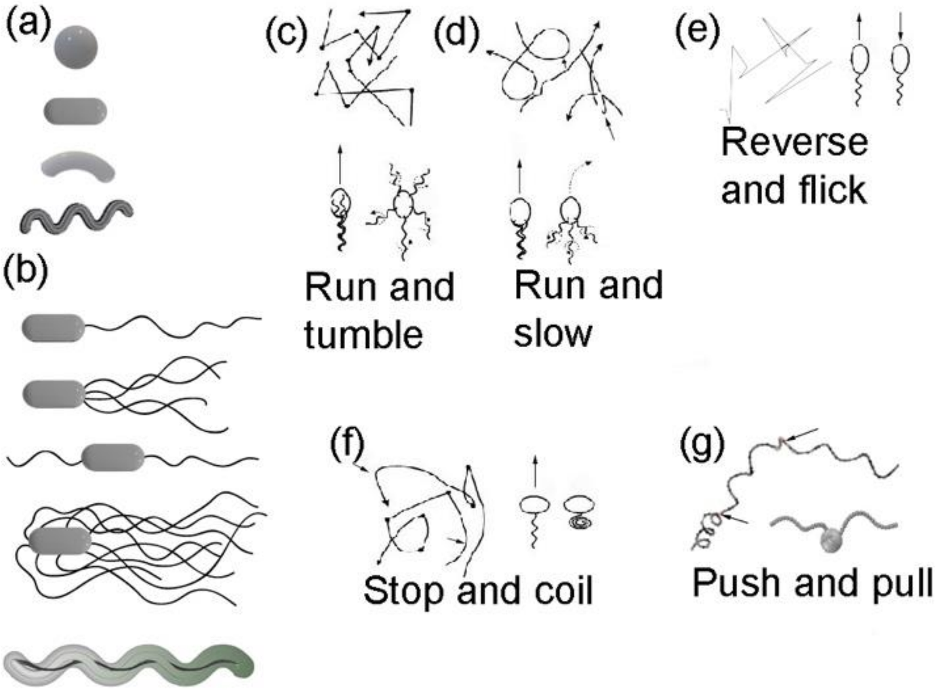

Figure 1. Cell morphologies and swimming patterns. (a) Both bacteria and archaea show a variety of body shapes that can be classified as cocci (spherical), bacilli (rods), curved rods, or spirals. (b) Flagella and archaella may be attached to the cell in a variety of patterns. A rod-shaped body is shown for simplicity, but the different flagellar patterns are seen across body types. From top to bottom are monotrichous (a single flagellum, which may be lateral or polar), lophotrichous (multiple flagella attached at a single point), amphitrichous (flagella on each end), peritrichous (multiple flagella attached at different points all over the surface), and periplasmic (flagella enclosed in the periplasmic space). (c) Run-and tumble pattern and (d) Run-and slow pattern (from (Armitage and Schmitt, 1997)[6]). (e) Reverse and flick. (f) Stop and coil (from (Armitage and Schmitt, 1997)[6]). (g) Push and pull (adapted from (Bente et al., 2020)).

2.0 Imaging and Motility

The world of biological cell imaging and tracking is vast, and much effort has been devoted to forwarding its development. Cells of interest range in size from multicellular eukaryotes such as *C. elegans* (1 mm), to single-cellular eukaryotes such as *Euglena* (50 µm), and finally to prokaryotes such as *E. coli* (1-2 µm). Additionally, cell tracking is of great interest in biomedical applications including leukocytes and red blood cells.

“Microswimmers” may also refer to non-living particles. Many studies have been conducted on microspheres[21-23]. Although microspheres can be used to approximate bacteria in size, their lack of self-motility simplifies data processing in ways that are not possible for bacteria. As such, we will limit the scope of this review to tracking of motile organisms on the order of 1-2 μm and the unique challenges these present.

We can divide the process of experimentally quantifying motility into three steps: 1. Choosing a microscopy technique to image samples, 2. Recording apparatus and software, and 3. Data analysis and tracking.

2. 1 Microscopy Techniques

Throughout the years, a variety of imaging techniques have been employed with the goal of bacterial tracking. These include phase contrast microscopy, darkfield microscopy, fluorescence microscopy, and digital holographic microscopy (both in-line and off-axis). Each system has tradeoffs as discussed below.

Phase Contrast Microscopy

Phase contrast microscopy is a standard technique found in most microbiology laboratories and easily implemented on all commercial microscopes. Depending upon the objective lens chosen, it is capable of either high resolution or fairly large depth of field. Diffraction-limited lateral (XY) resolution is given by λ/NA, where λ is the wavelength of illuminating light and NA is the numerical aperture of the objective. Depth of field d is the sum of two terms, a wave term and a geometrical optical term:

$$d = \frac{n\lambda}{(NA)^2} + \frac{ne}{M(NA)},$$

where n is index of refraction of the medium between the lens and the coverslip (air or immersion oil), e is the smallest resolvable element, and M is the magnification. (**Figure 2**).

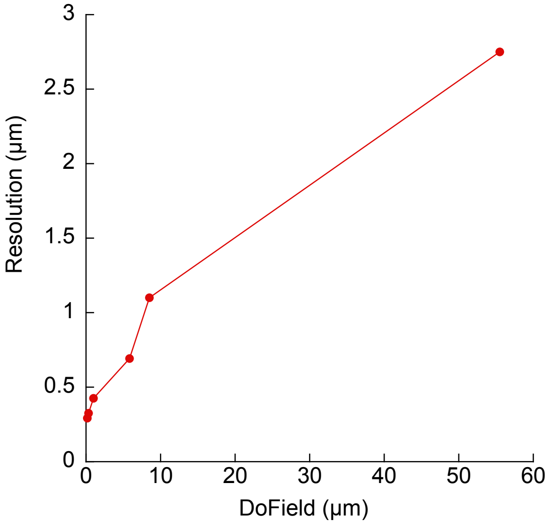

Figure 2. Tradeoff between resolution and depth of field for 550 nm illumination and air objectives. The non-linear relationship can be appreciated by observing that for bacterial cells on the order of 1 µm, the ability to resolve the cells will lead to a depth of field of < 10 µm, whereas a decrease of resolution for 2.5 µm will permit a depth of field of > 50 µm.

Phase contrast microscopy represents one of the most established and successful methods of bacterial tracking. It has been used for some significant recent results, such as tracking a variety of swimming archaea, including hyperthermophiles [24] and discovery of the importance of cell body motion in swimming of Caulobacter [25].

The primary disadvantage of phase contrast microscopy is that cells are lost as they swim in X and Y, or out of focus in the Z plane. Manual manipulation or digital tracking stages may be used to follow cells. Methods to follow single cells include the use of scanning stages [26-28] or scanning objectives [29]. These methods are limited by their scanning speed. Most recently, a technique has been proposed for determining Z depth in out-of-focus organisms by fitting the Airy ring pattern to calibrated patterns from test cells[30].

In some experiments, it is not necessary to permit the cells to swim freely in Z. In this case, sample chambers or flow cells may be constructed that restrict the cells to a single focal plane. This is useful when only 2D motion is necessary, such as to determine the fraction of motile cells or a general idea of the swimming speed. This may be useful for determining cell health or growth phase [31].

Digital Holographic Microscopy

Digital holographic microscopy (DHM) is a volumetric technique based upon interferometry, where a volume of view is captured in a single snapshot (hologram). The hologram appears as a pattern of Airy rings indicating out-of-focus objects throughout the focal depth. The typical approach to analyzing DHM data is to reconstruct the optical field through a chosen Z depth and spacing based upon the hologram. Reconstruction methods depend upon the DHM geometry used, namely “off-axis”, where object and reference beams interfere at an angle (**Figure 3A**), or “inline” imaging (DIHM) where a single beam serves as both object and reference (**Figure 3B**).

Off-axis holography separates the spatial frequencies from the unscattered “direct term” as well as separating the real and virtual images from one another, facilitating ease of reconstruction into both amplitude and quantitative phase images. Amplitude images are equivalent to transmission light microscopy; quantitative phase images have no direct counterpart in ordinary light microscopy and are related to the product of the cell thickness *h* and the difference in refractive index between the medium (n_m) and cell (n_c). The lateral resolution of DHM is equivalent to that of brightfield microscopy. Reconstruction of DIHM images is more complicated, since the direct term is not readily filtered out, leading to "ghost" images. Nonetheless, many algorithms have been developed for reconstruction and phase retrieval from these images [32-36].

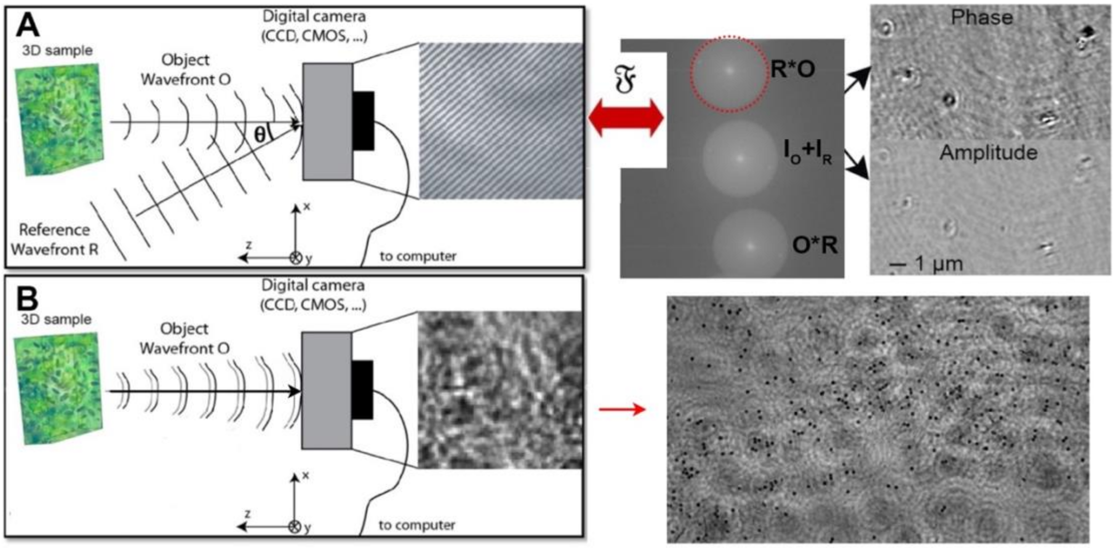

Figure 3. Off-axis DHM and DIHM. (A) Off-axis holography uses the interference of two coherent beams of light from a single source to record the complete sample volume in each captured frame. The "object" beam passes through the sample, while the "reference" beam takes an identical-length unperturbed path to the detector. The two beams are interfered at the detector array and the resulting interference pattern records the phase and amplitude of the object beam. Numerical refocusing allows reconstruction of phase and amplitude images through the depth of the sample. (B) Digital in-line holographic microscopy (DIHM) uses a single beam which is assumed to be slightly perturbed by the object and interferes with itself. The resulting hologram does not capture information as fringes. The illustrated reconstruction method shows a dark-field-like reconstruction that works for phase, amplitude, and phase-amplitude objects (hologram and reconstruction are adapted from (https://www.sciencedirect.com/science/article/pii/S0143816620300762) under terms of the Creative Commons license; the images were cropped).

The limit to the depth that can be reconstructed from DHM results from a degradation of spatial resolution as the reconstruction propagator extends outside the focal plane. For typical bacterial imaging experiments with ~1 μm spatial resolution, the depth of the sample is limited to ~1 mm, which is very large compared with other microscopic techniques and which represents the biggest advantage of this imaging technique, allowing a simultaneous snapshot of essentially an unconstrained volume. Acquisition rates are limited by the camera frame rate. As a result of this major advantage, a large number of recent papers have reported prokaryotic tracking using DHM (see **Table 1**). The optics of DHM are also simple and the hardware is low in cost.

The disadvantage of DHM is a generally low signal-to-noise caused by the extreme sensitivity of the technique to aberrations in the optics and/or sample chamber, and the intrinsic low contrast of most prokaryotic cells in amplitude and phase. A large amount of research has gone into development of experimental and software techniques for improvement of DHM contrast. Digital aberration correction is essential, either by use of reference holograms[37] or by median subtraction of images or of raw holograms prior to reconstruction (**Figure 4**) [38,39]. These techniques remove motionless objects, which can be an advantage or a disadvantage depending upon the experiment. Some dyes can also increase contrast for DHM, but this is an area that has not been well explored [40]. The development of agents for specific enhancement of phase contrast has also been little studied, though it is possible through labeling techniques such as genetically encoded air-filled vesicles which provide substantial change in refractive index relative to aqueous medium [41].

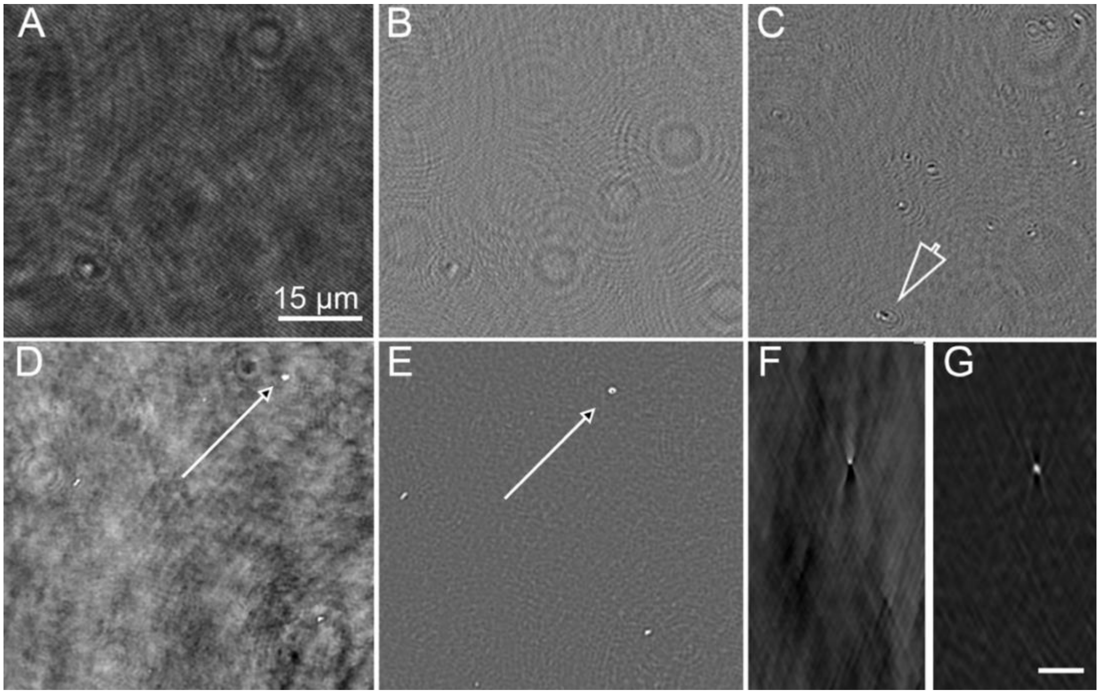

Figure 4. Appearance of bacteria (in this case, the marine organism *Collwellia psychrerythraea* 34H) under DHM with and without denoising. (A) Raw hologram of part of the microscopic field of view. (B) Median subtracted hologram (as in REF) showing individual cells whose Airy patterns overlap in Z. (C) Reconstruction on a single focal plane in amplitude. Cells in focus (arrow) are reduced to 1-2 pixels, while cells not in focus in that plane retain large diffraction patterns. (D) Phase reconstruction on a single Z plane, with an example cell indicated by an arrow. (E) Phase gradient (REF) at the same plane. (F) YZ image through a stack of raw phase images reconstructed every 1 µm. (G) Derivative image of cell in the *yz* plane.

DHM leads to large datasets and its analysis is computationally intensive. A 30 second dataset at 15 frames/s and 4 Mpx yields 1.5 GB of images before reconstruction. Depending upon the z-spacing selected for reconstruction, a full reconstructed dataset may be upwards of 1 Tb. Few software packages available for analysis. Commercial software is usually tied to a specific instrument. Open-source Fiji for both in-line and off-axis DHM have recently been reported [42] [43].

An alternative to reconstruction is to extract Z information directly from the holograms. If the form of the diffraction pattern or the Z-position of the object are known, the Airy pattern may be easily fit to a function based upon Lorenz-Mie theory [44-46]. For more complex shapes, a discrete dipole approximation must be used[47]. Open-source software is available to perform these fits, but this approach is highly complex and computationally intensive when neither the exact shape and size nor the axial depth are known. Good signal to noise is also essential to permit accurate fitting of the patterns. This approach has been used to track runs and tumbles in *E. coli* [48] (**Figure 5**).

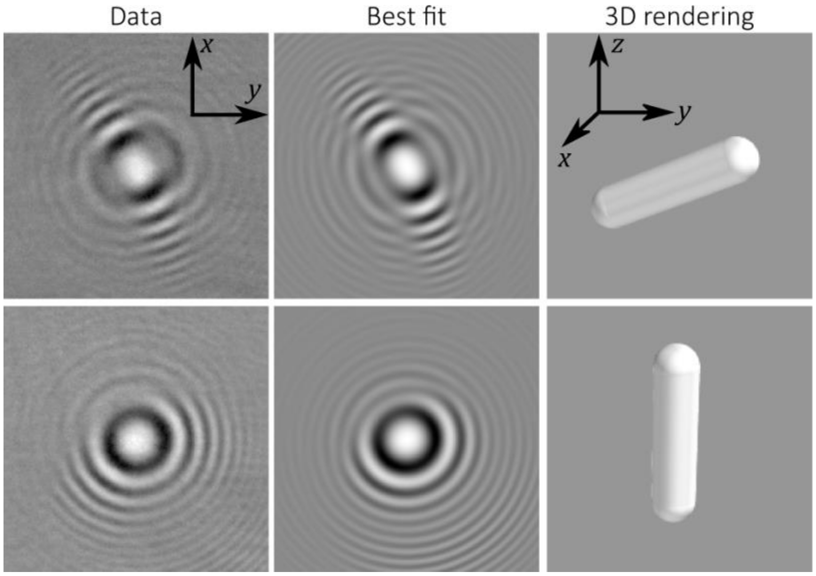

Figure 5. Holograms of freely swimming *E. coli* in a time series. Two frames are shown in the left column, where the asymmetry in the fringes is noticeably different between the frames. The best-fit holograms are shown in the middle, and three-dimensional renderings from the best-fit holograms are shown on the right using the discrete dipole approximation and the software HoloPy ((http://manoharan.seas.harvard.edu/holopy/). (Image from: Anna Wang, Rees F. Garmann, Vinothan N. Manoharan, “Tracking runs and tumbles with scattering solutions and digital holographic microscopy,” Opt. Express **24,** 23719-23725 (2016); © 2016 Optical Society of America. Image not edited).

Recent findings using DHM are summarized in **Table 1**.

Table 1: Digital Holographic Microscopy and Bacterial Motility

Paper	**Objective(s)**	**Wavelength**	**Camera**	**Organism Studied**	**Tracking Method**
Wang et al. *Optics Express* **2016,** 24, (21), 23719-23725.	60x NA=1.2	660nm	Photon Focus MVD-1024E-160, 100fps	*E. coli*	HoloPy
Qi et al. *Langmuir* **2017,** 33, (14), 3525-3533.	40x NA=0.6	455nm	sCMOS 20Hz for 2min	*E. coli*	Trajectories linked by home-made Python code
Marin et al. *Methods* **2018,** 136, 60-65	NA=0.3	405nm	170ms intervals for 3min	*S. marcescens*	Manual Tracking / 2D WTMM segmentation method
Huang et al. *Optics Express* **2018,** 26, (8), 9920-9930.	40x NA=0.6 100x NA=1.4	455nm 450nm	sCMOS	*E. coli*	No tracking

Peng et al. *Langmuir* **2019,** 35, (37), 12257-12263.	40x NA=0.6	455nm	sCMOS 20fps	*E. coli* *Pseudomonas*	Coordinates from Rayleigh-Sommerfeld propagation/Trajectories from homemade program
Hook, et al. *Msystems* **2019,** 4, (5).	60x NA=1.4	685nm	CMOS 41.6Hz	*P. aeruginosa*	Bacterial trajectory: bespoke Matlab scripts: DHMTracking and StackMaster
Wang et al. *Optics Express* **2020,** 28, (19), 28060-28071.	40x NA=0.6	505nm	sCMOS 50fps/2min	*E. coli*	Image recognition 3D tracking method
Kuhn et al. *Nat Commun* **2018,** 9, (1), 5369	10x NA=0.3	642 nm	Mikrotron MC-1362 CMOS 50 fps	*Shewanella putrefaciens*	Median division followed by reconstruction to extract cell coordinates; assembly of tracks using custom software
Vater et al. *PLoS One* **2014,** 9, (1), e87765.	20x NA 0.4 In-line	532 nm	pco.imaging CMOS 5 fps	*Pseudomonas aeruginosa*	Median subtraction; reconstruction and projection into XY, XZ, and YZ; polynomial regression smoothing

Fluorescence Microscopy

Fluorescence microscopy has the highest signal-to-noise of any of the discussed microscopic techniques. It has a higher effective resolution than other techniques because of reduced noise as well as the ability of targeted probes to highlight small structures, such as flagella, that are ordinarily below the diffraction limit. While some dyes might affect motility[49,50], the advantages of fluorescence make it essential whenever high resolution or high signal-to-noise are needed.

At the whole-cell level, the ability to genetically modify bacteria to express fluorescent proteins (FPs) such as green fluorescent protein (GFP) and its variants has enabled numerous tracking experiments in both simple and complex milieux. FPs have little effect on physiology and demonstrate low phototoxicity, permitting them to be used for long-term recordings, although care should be taken to use green light rather than blue or violet for excitation, as the shorter wavelengths affect cell growth [51]. Green excitation corresponds to Yellow Fluorescent Protein (YFP) emission; YFP is very commonly used in microbial studies. The GFP family of proteins requires oxygen for maturation and thus cannot be used in anaerobes; a variety of oxygen-independent alternatives have emerged recently [52-54].

For observation of flagella, fluorescence microscopy with labeling is essential. Fluorescence has been used to observe correlate flagellar movements with tumbles in E. coli, B. subtilis, and motile Enterococcus [55]. Cells were labeled with Alexa Fluor 532, and an overlay of phase contrast and fluorescence was used to visualize the cell bodies and flagella (**Fig. 6A**). Fluorescent labeling of flagella may also be used to provide complementary information for cells tracked by other means. One study examining the distribution of flagellar filaments FlaA and FlaB used fluorescent labeling of inserted cysteine residues to visualize the flagella in individual cells, then used DHM without labeling for high-throughput tracking (**Fig. 6B**) [56].

The biggest drawback for long-term fluorescence microscopy is photobleaching. Photobleaching may be reduced by limiting light intensity and/or exposure times or by the addition of antioxidants to the medium (or the removal of oxygen if possible) [57-59].

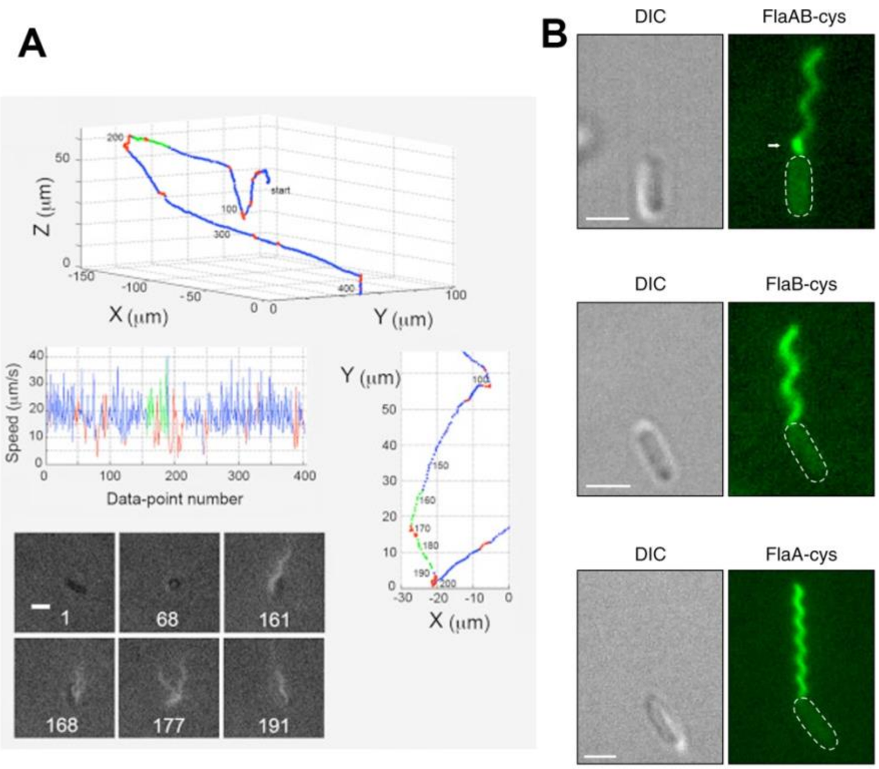

Figure 6. Fluorescence microscopy and flagellar labelling. Use of fluorescence microscopy and flagellar labeling to elucidate the role of flagella in swimming. (A) Track of a typical untreated *E. coli* cell (*upper panel*) with combined phase-contrast and fluorescence images (*dark* and *light*, respectively, *lower-left panel*). Runs are shown in blue, tumbles are in red, and runs with the laser on are in green. Each data point along the trajectory corresponds to one video frame (30/s). At the start, image 1 (*lower-left panel*), the phase-contrast image shows the cell moving parallel to the *X*-*Y* image plane. Cell-body measurements were made from this image. At image 68, the cell is seen end-on while moving along the *Z* axis at track point 68. The overview (*right panel*) shows the track in the *X*-*Y* plane

from points 100–200, and includes laser illumination points 157–191. The cell was running with a tight bundle in image 161. A tumble occurred during points 168–177. In image 177, as the tumble ended, the bundle started to reform, a process that was completed at point 188 (not shown). A tightly formed bundle is evident in image 191. After this point, another tumble began. The scale bar is 2 μm (FromBiophys J. 2016 Aug 9; 111(3): 630–639. doi: 10.1016/j.bpj.2016.05.053, © 2016 Biophysical Society, used with permission). (B) Micrographs of cells with fluorescently labeled flagellar filaments displaying the outcome of the genetic editing of the flagellin genes (from Kuhn et al, 2018, under terms of the Creative Commons license).

Recent findings using DHM are summarized in **Table 2**.

Table 2: Fluorescence microscopy and bacterial tracking

Paper	**Objective(s)**	**Fluorophore**	**Camera**	**Organism Studied**	**Tracking Method**
Figueroa-Morales et al. *Physical Review X* **2020,** 10, (2), 021004.	100x/ NA 0.9	Yello fluorescent protein YFP	ANDOR iXon 897 EMCCD (30 fps at 512x512)	*E. coli*	Lagrangian tracker (motorized stage, photobleaching correction)
Vizsnyiczai et al *Nat Commun* **2020,** 11, (1), 2340.	60x/NA 1.27	Red fluorescent protein mRFP1	Hamamatsu Orca Flash 4.0 (50 fps)	E. coli	Custom software, confined channels
Khong et al. *bioRxiv* **2020**, 2020.05.03.075507.	40x, NA 1.0	Vybrant Dyecycle Green	Zeiss, 80 ms exposure	E. coli P. aeruginosa	Segmentation and LAP tracking

Turner et al. *Biophysical Journal* **2016,** 111, (3), 630-639.	25x LWD/ NA 1.1	Alexa Fluor 532 maleimide (flagellar labeling)	KPC-650BH (30 fps)	E. coli B. subtilis Enterococcus	Tracking microscope

2.2 Recording Apparatus and Software

Cameras

Commercially available cameras require trade-offs between field of view and framerate. Until recently, obtaining full 2048x2048 or even 1024 x 1024 pixel images at >50 frames/s required highly specialized and costly instrumentation. Although fast cameras are becoming more readily available, obtaining frame rates >50 fps usually requires some downsampling as well as limiting any simultaneous data imaging. Cameras for fluorescence represent a special category, as they must be extremely sensitive and have low background; most are cooled. If specialized wavelengths such as ultraviolet or infrared are imaged, this imposes additional demands upon the camera. Because of the complexity of the trade-offs, we have identified the camera model in all of the studies identified in Tables 1 and 2.

Acquisition Software

Acquisition software is dependent on the microscopy technique chosen. For most applications, the camera software is sufficient; a software development kit (SDK) is usually provided with camera purchase. Manufacturers often sell software separately, but the cost of the software often exceeds that of the camera. The open-source package

MicroManager has been developed to interface with a large number of commercial cameras, microscopes, and accessories in order to minimize costs associated with software.

For specialized techniques such as DHM, software is usually custom. Several research groups, including our own, have made their DHM software openly available.

Off-axis DHM (JPL; our collaboration): https://github.com/dhm-org/dhm_suite

In-line DHM

https://2017.igem.org/Team:TU_Darmstadt/tech/software

http://www.rowland.harvard.edu/rjf/wilson/Downloads.html

https://physics.nyu.edu/grierlab/software.html#hvm

3.0 Cell Tracking and Bacterial Motility

Cell tracking in 2D and 3D consists of 1) preprocessing the images, 2 detecting the cells and 3) linking them correctly in successive video frames.

General Considerations

Software may be open-source or commercial. Choices are determined by the project's budget as well as any needs to re-tune available code to custom optical systems. The platform ImageJ (FIJI) [60]is highly versatile, open source, and widely used by biologists, so in this review we will mention when a FIJI package or plug-in exists for a particular technique. Many packages for MATLAB are also available, as well as custom programs based in Python. An example of Python-based software is the Holographic Examination for Lifelike Motility (HELM), developed by the Jet Propulsion Laboratory.

Preprocessing

The preprocessing necessary is highly dependent upon the technique used. For most brightfield and phase contrast techniques, some sort of background subtraction using different denoising approaches (rolling ball algorithm, median, Gaussian filter) is necessary. Such filters are found in all common image-processing software packages, both open-source and commercial.

For DHM, aberration correction is usually done as part of reconstruction, using the same software package. The denoising approaches to amplitude and phase images are different. Quantitative phase retrieval presents specific challenges; approaches to phase aberration correction have been recently reviewed [61]. While amplitude images are generally noisier than phase images, especially with respect to speckly noises, approaches to de-noising are simpler. If the fringes are temporally stable, the hologram may be median subtracted before reconstruction in amplitude [39]. Alternatively, amplitude images may be median subtracted plane-by-plane after reconstruction. For motile objects, this usually results in sufficient de-noising for segmentation.

For 3D datasets, deconvolution may be necessary to improve axial resolution, which is lower than lateral resolution for all microscopic techniques. Deconvolution is based upon knowing the shape of the point-spread function (PSF) for the microscope system, and reducing each PSF in the image to a point based upon this input. The PSF may be experimentally measured by imaging unresolved point particles, or may be theoretically calculated based upon the optics of the microscope. Commercial packages and open-source plug-ins are available for deconvolution of fluorescence images. Two specific packages exist for Fiji: DeconvolutionLab2 [62] and Iterative Deconvolve 3D (https://imagej.net/plugins/iterative-deconvolve-3d).

Segmentation

Cell detection consists of recognizing pixel clusters of a defined size, which stand out from the background in a way that may be identified by an algorithm. Frequently, but not always, images are thresholded and converted to binary before tracking. Segmentation of fluorescence images is fairly straightforward, but for low signal-to-noise techniques such as brightfield and DHM, segmentation may be the most challenging aspect of the data analysis. A recent review provided a detailed overview of techniques and software for microbial segmentation [63], so for purposes of this discussion, we will refer to and build upon this article without covering segmentation in depth. We do, however, emphasize its importance as the first step in nearly all approaches to tracking.

Tracking

While excellent tools exist for analyzing passive motion, such as Brownian motion, simple techniques such as nearest neighbor linking over the smallest Euclidean distance cannot be used for particle tracking with partly fast-moving, strongly accelerating microbes. Particle tracks intersect and overlap, and velocity vectors are unpredictable. Therefore, the linking step is often done using a cost (or energy) function that takes into account velocity aspects (such as smoothness of the trajectory segment, smoothness of 3-d velocity, smoothness, and upper bound conditions on accelerations) or morphological characteristics (cell size, shape, aspect). However, the correct weighting of all the different features of the cost function is often highly dependent on the used set-up and requires a lot of fine-tuning.

Creating and finding tools for cell tracking is an open question. In fact, in 2013 the first edition of a "Cell Tracking Challenge" was hosted by the IEEE International Symposium on Biomedical Imaging (ISBI). As the authors stated, "at present, there exists no universally best method for particle tracking" and this is still valid today, a decade later.

Large datasets are generated from imaging and recording samples. One of the primary challenges for bacterial tracking relates to its low signal to noise ratios. There are a variety of both in-house and commercially available software packages that attempt to solve this problem. However, there is currently no "black-box" solution that works for any bacterial dataset.

Manual tracking

Manual tracking was the only possible approach before the development of high-performance computers [64,65]. Even with modern computation, it is still in widespread use, either as a stand-alone technique or to "ground truth" automated methods. Computational tools can assist with manual tracking by annotating and saving tracks. The technique is tedious, and is frequently outsourced to data analysts or assigned to undergraduate students. Throughput is low.

Automated detection and tracking

Automated tracking greatly decreases the workload and improves statistics. A large body of literature exists on tracking bacteria, with no one program applicable to all cases. Open-source, extensible platforms such as TrackMate [66] can help consolidate different approaches to segmentation and linking in order to determine the best approach for a particular dataset. TrackMate has recently been integrated directly with segmentation algorithms [67].

Despite the availability of these tools, optimizing parameters can be time-consuming or even futile. Differences in noise or cell density from frame to frame, and changes in bacterial appearance with tumbling or other motions, can lead to fragmented tracks and poor classification. Machine learning approaches can help to optimize the many parameters needed for effective tracking, though the training can be extensive and highly dataset-dependent [68-70] [71]. A recent paper proposed an adaptive kernel model [72]for addressing these challenges and applied it to *E. coli*. For all of these methods, generalizability is challenging; what works for *E. coli* often does not work with smaller, faster species, such as *Vibrio*.

DDM

Differential dynamic microscopy (DDM) is a recent method (introduced in 2008 and developed for bacteria in 2011-2012 [73,74]) that allows critical motility parameters such as velocities and fraction of motile particles to be extracted from recordings with low signal to noise ratios. DDM uses successive images to characterize the motility of a population by calculating the temporal fluctuations of the number density over different length scales. The key parameter is the differential image correlation function (DICF),

$g(q,\tau)$, which is the modulus of the difference of two Fourier-space images over a time step τ:

$$g(q,\tau) = \langle |I(q,t+\tau) - I(q,t)|^2 \rangle_t.$$

The DICF is related to the intermediate scattering function (ISF), $f(q, \tau)$, by

$$g(q, \tau) = A(q)[1 - f(q, \tau)] + B(q),$$

where $A(q)$ depends on the optics, particle shape, and mutual arrangement, and $B(q)$ represents the camera noise. For a mixed population of motile- and non-motile cells with motile fraction α, the ISF consists of a part due to Brownian motion, represented by the diffusion coefficient D, and a part due to swimming:

$$f(q,\tau) = (1-\alpha)e^{-q^2 D\tau} + \alpha e^{-q^2 Dt} \int_0^\infty dv P(v) \frac{sin(qv\tau)}{qv\tau},$$

where P(v) is the velocity distribution function. The term due to swimming decorrelates much more quickly than that due to Brownian motion, resulting in a two-phase f that may be fit to a multi-parameter function to extract the diffusion coefficient, mean swimming speed, and fraction swimming. The advantages of this method are rapid, tracking-free determination of these key motility parameters. The disadvantages are lack of visualization, so that spurious results are difficult to identify; some comparison with manual tracking is needed. In addition, a form for the velocity distribution function needs to be specified, so some advance knowledge of swimming characteristics is needed. The technique also requires a large data volume, approximately 1000 frames at 50 frames/s for cells swimming at typical run-and-tumble speeds (10-50 µm/s).

Analyzing tracks

Unlike simple physical motion such as Brownian motion, active motility displays both physical and physiological features that have not been fully elucidated. As one example, the run-reverse-flick swimming pattern of bacteria with a single polar flagellum was not described until 2011 [75]. Persistence in tracks was first reported in 2013 [76]. The biophysics underlying bacterial motility can be lost if tracks are fragmented, spurious, or if they miss key features such as reorientation events. Because of the different possible motility patterns as shown in Fig. 1, such analysis must be strain-dependent. This becomes increasingly challenging if the culture represents a mix of species.

4.0 Conclusion

Tracking bacteria still represents a challenge, especially in 3D or under extreme conditions such as high or low temperature, high cell speed, or dense or inhomogeneous cultures (mixed species or phenotypes). Each experimental type, or even each dataset, will require customized methods and ground-truthing to eliminate false negatives and false positives. Manual tracking remains a necessary task for many applications, since the human eye and brain can identify cells and motion in noisy environments where even the most sophisticated algorithms fail.

References

1 Berg, H. C. How to Track Bacteria. *Review of Scientific Instruments* **42**, 868-871, doi:10.1063/1.1685246 (1971).

2 Miyata, M. *et al.* Tree of motility – A proposed history of motility systems in the tree of life. *Genes to Cells* **25**, 6-21, doi:10.1111/gtc.12737 (2020).

3 Albers, S. V. & Jarrell, K. F. The archaellum: how Archaea swim. *Front Microbiol* **6**, 23, doi:10.3389/fmicb.2015.00023 (2015).

4 Albers, C. N., Kramshøj, M. & Rinnan, R. Rapid mineralization of biogenic volatile organic compounds in temperate and Arctic soils. *Biogeosciences* **15**, 3591-3601, doi:10.5194/bg-15-3591-2018 (2018).

5 Bardy, S. L., Briegel, A., Rainville, S. & Krell, T. Recent Advances and Future Prospects in Bacterial and Archaeal Locomotion and Signal Transduction. *Journal of Bacteriology* **199**, JB.00203-00217, doi:10.1128/jb.00203-17 (2017).

6 Armitage, J. P. & Schmitt, R. Bacterial chemotaxis: Rhodobacter sphaeroide and Sinorhizobium meliloti - variations on a theme? *Microbiology* **143**, 3671-3682, doi:10.1099/00221287-143-12-3671 (1997).

7 Stocker, R. Reverse and flick: Hybrid locomotion in bacteria. *Proceedings of the National Academy of Sciences* **108**, 2635-2636, doi:10.1073/pnas.1019199108 (2011).

8 Armitage, J. P. in *Advances in Microbial Physiology* Vol. 41 (ed R. K. Poole) 229-289 (Academic Press, 1999).

9 Zhang, Y.-G., Wu, S., Xia, Y. & Sun, J. Salmonella -infected crypt-derived intestinal organoid culture system for host-bacterial interactions. *Physiological Reports* **2**, e12147, doi:10.14814/phy2.12147 (2014).

10 Tahara, Y. *et al.* Gut Microbiota-Derived Short Chain Fatty Acids Induce Circadian Clock Entrainment in Mouse Peripheral Tissue. *Scientific Reports* **8**, doi:10.1038/s41598-018-19836-7 (2018).

11 Najafi, J. *et al.* Flagellar number governs bacterial spreading and transport efficiency. *Science Advances* **4**, eaar6425, doi:10.1126/sciadv.aar6425 (2018).

12 Waterbury, J. B., Willey, J. M., Franks, D. G., Valois, F. W. & Watson, S. W. A cyanobacterium capable of swimming motility. *Science* **230**, 74-76, doi:10.1126/science.230.4721.74 (1985).

13 Piepenbrink, K. H. *et al.* Structural Diversity in the Type IV Pili of Multidrug-resistant Acinetobacter. *Journal of Biological Chemistry* **291**, 22924-22935, doi:10.1074/jbc.m116.751099 (2016).

14 Nan, B. & Zusman, D. R. Novel mechanisms power bacterial gliding motility. *Molecular Microbiology* **101**, 186-193, doi:10.1111/mmi.13389 (2016).

15 Holscher, H. D. Dietary fiber and prebiotics and the gastrointestinal microbiota. *Gut Microbes* **8**, 172-184, doi:10.1080/19490976.2017.1290756 (2017).

16 Pollitt, E. J. G. & Diggle, S. P. Defining motility in the Staphylococci. *Cellular and Molecular Life Sciences* **74**, 2943-2958, doi:10.1007/s00018-017-2507-z (2017).

17 Herzog, B. & Wirth, R. Swimming Behavior of Selected Species of Archaea. *Applied and Environmental Microbiology* **78**, 1670-1674, doi:10.1128/aem.06723-11 (2012).

18 Schuech, R., Hoehfurtner, T., Smith, D. J. & Humphries, S. Motile curved bacteria are Pareto-optimal. *Proceedings of the National Academy of Sciences* **116**, 14440-14447, doi:10.1073/pnas.1818997116 (2019).

19 Yuan, K., Jurado-Sánchez, B. & Escarpa, A. Dual-Propelled Lanbiotic Based Janus Micromotors for Selective Inactivation of Bacterial Biofilms. *Angewandte Chemie International Edition* **60**, 4915-4924, doi:10.1002/anie.202011617 (2021).

20 Gahlmann, A. & Moerner, W. E. Exploring bacterial cell biology with single-molecule tracking and super-resolution imaging. *Nat Rev Microbiol* **12**, 9-22, doi:10.1038/nrmicro3154 (2014).

21 Lei, H. *et al.* Nano-level position resolution for particle tracking in digital in-line holographic microscopy. *Journal of Microscopy* **260**, 100-106, doi:10.1111/jmi.12271 (2015).

22 Zhang, H., Stangner, T., Wiklund, K., Rodriguez, A. & Andersson, M. UmUTracker: A versatile MATLAB program for automated particle tracking of 2D light microscopy or 3D digital holography data. *Computer Physics Communications* **219**, 390-399, doi:10.1016/j.cpc.2017.05.029 (2017).

23 Lee, S.-H. *et al.* Characterizing and tracking single colloidal particles with video holographic microscopy. *Optics Express* **15**, 18275-18282, doi:10.1364/OE.15.018275 (2007).

24 Herzog, B. & Wirth, R. Swimming behavior of selected species of Archaea. *Appl Environ Microbiol* **78**, 1670-1674, doi:10.1128/AEM.06723-11 (2012).

25 Liu, B. *et al.* Helical motion of the cell body enhances Caulobacter crescentus motility. *Proc Natl Acad Sci U S A* **111**, 11252-11256, doi:10.1073/pnas.1407636111 (2014).

26 Yang, T. *et al.* Rapid imaging of large tissues using high-resolution stage-scanning microscopy. *Biomed Opt Express* **6**, 1867-1875, doi:10.1364/BOE.6.001867 (2015).

27 Berg, H. C. & Brown, D. A. Chemotaxis in Escherichia coli analyzed by three-dimensional tracking. *Antibiot Chemother (1971)* **19**, 55-78, doi:10.1159/000395424 (1974).

28 Frymier, P. D., Ford, R. M., Berg, H. C. & Cummings, P. T. Three-dimensional tracking of motile bacteria near a solid planar surface. *Proc Natl Acad Sci U S A* **92**, 6195-6199, doi:10.1073/pnas.92.13.6195 (1995).

29 Corkidi, G., Taboada, B., Wood, C. D., Guerrero, A. & Darszon, A. Tracking sperm in three-dimensions. *Biochem Biophys Res Commun* **373**, 125-129, doi:10.1016/j.bbrc.2008.05.189 (2008).

30 Taute, K. M., Gude, S., Tans, S. J. & Shimizu, T. S. High-throughput 3D tracking of bacteria on a standard phase contrast microscope. *Nature Communications* **6**, doi:10.1038/ncomms9776 (2015).

31 Ziegler, A. *et al.* Single bacteria movement tracking by online microscopy--a proof of concept study. *PLoS One* **10**, e0122531, doi:10.1371/journal.pone.0122531 (2015).

32 Wang, H., Lyu, M. & Situ, G. eHoloNet: a learning-based end-to-end approach for in-line digital holographic reconstruction. *Optics express* **26**, 22603-22614 (2018).

33 Latychevskaia, T. & Fink, H.-W. Simultaneous reconstruction of phase and amplitude contrast from a single holographic record. *Optics Express* **17**, 10697-10705 (2009).

34 Zhang, Y., Pedrini, G., Osten, W. & Tiziani, H. J. Whole optical wave field reconstruction from double or multi in-line holograms by phase retrieval algorithm. *Optics Express* **11**, 3234-3241 (2003).

35 Micó, V., García, J., Camacho, L. & Zalevsky, Z. in *Coherent Light Microscopy: Imaging and Quantitative Phase Analysis* (eds Pietro Ferraro, Adam Wax, & Zeev Zalevsky) 145-167 (Springer Berlin Heidelberg, 2011).

36 Galande, A. S., Thapa, V., Ram, H. P. & John, R. in *OSA Imaging and Applied Optics Congress 2021 (3D, COSI, DH, ISA, pcAOP).* (eds H. Javidi B. Martinez-Corral M. Matoba O. Stern A. Thibault S. Alieva T. Ke J. Willomitzer F. Okten F. Silveira P. Banerjee P. Stoykova E. Chu D. Park J. Imai F. Joo C. Digman M.

Gardner D. Gladysz S. LeMaster D. Basu S. Hua & O. Korotkova) CTh7A.7 (Optica Publishing Group).

37 Colomb, T. *et al.* Total aberrations compensation in digital holographic microscopy with a reference conjugated hologram. *Opt Express* **14**, 4300-4306, doi:10.1364/oe.14.004300 (2006).

38 Gibson, T., Bedrossian, M., Serabyn, E., Lindensmith, C. & Nadeau, J. L. Using the Gouy phase anomaly to localize and track bacteria in digital holographic microscopy 4D images. *J Opt Soc Am A Opt Image Sci Vis* **38**, A11-A18, doi:10.1364/JOSAA.404004 (2021).

39 Bedrossian, M., Wallace, J. K., Serabyn, E., Lindensmith, C. & Nadeau, J. Enhancing final image contrast in off-axis digital holography using residual fringes. *Opt Express* **28**, 16764-16771, doi:10.1364/OE.394231 (2020).

40 Nadeau, J. L., Bin Cho, Y., Kuhn, J. & Liewer, K. Improved Tracking and Resolution of Bacteria in Holographic Microscopy Using Dye and Fluorescent Protein Labeling. *Frontiers in Chemistry* **4**, doi:10.3389/fchem.2016.00017 (2016).

41 Farhadi, A. *et al.* Genetically Encoded Phase Contrast Agents for Digital Holographic Microscopy. *Nano Letters* **20**, 8127-8134, doi:10.1021/acs.nanolett.0c03159 (2020).

42 Buitrago-Duque, C. & Garcia-Sucerquia, J. Realistic simulation and real-time reconstruction of digital holographic microscopy experiments in ImageJ. *Appl. Opt.* **61**, B56-B63, doi:10.1364/AO.443137 (2022).

43 Cohoe, D., Hanczarek, I., Wallace, J. K. & Nadeau, J. Multiwavelength Digital Holographic Imaging and Phase Unwrapping of Protozoa Using Custom Fiji Plug-ins. *Frontiers in Physics* **7**, doi:10.3389/fphy.2019.00094 (2019).

44 Cheong, F. C. *et al.* Flow visualization and flow cytometry with holographic video microscopy. *Opt Express* **17**, 13071-13079, doi:10.1364/oe.17.013071 (2009).

45 Lee, S. H. *et al.* Characterizing and tracking single colloidal particles with video holographic microscopy. *Opt Express* **15**, 18275-18282, doi:10.1364/oe.15.018275 (2007).

46 Ruffner, D. B., Cheong, F. C., Blusewicz, J. M. & Philips, L. A. Lifting degeneracy in holographic characterization of colloidal particles using multi-color imaging. *Optics express* **26**, 13239-13251, doi:10.1364/OE.26.013239 (2018).

47 Wang, A. *et al.* Using the discrete dipole approximation and holographic microscopy to measure rotational dynamics of non-spherical colloidal particles. *Journal of Quantitative Spectroscopy and Radiative Transfer* **146**, 499-509, doi:https://doi.org/10.1016/j.jqsrt.2013.12.019 (2014).

48 Wang, A., Garmann, R. F. & Manoharan, V. N. Tracking E-coli runs and tumbles with scattering solutions and digital holographic microscopy. *Optics Express* **24**, 23719-23725, doi:10.1364/oe.24.023719 (2016).

49 Wainwright, M., Phoenix, D. A., Marland, J., Wareing, D. R. & Bolton, F. J. In-vitro photobactericidal activity of aminoacridines. *J Antimicrob Chemother* **40**, 587-589, doi:10.1093/jac/40.4.587 (1997).

50 Martin, J. P. & Logsdon, N. Oxygen radicals mediate cell inactivation by acridine dyes, fluorescein, and lucifer yellow CH. *Photochem Photobiol* **46**, 45-53, doi:10.1111/j.1751-1097.1987.tb04734.x (1987).

51 El Najjar, N. *et al.* Bacterial cell growth is arrested by violet and blue, but not yellow light excitation during fluorescence microscopy. *BMC Mol Cell Biol* **21**, 35, doi:10.1186/s12860-020-00277-y (2020).

52 Ko, S. *et al.* Discovery of Novel Pseudomonas putida Flavin-Binding Fluorescent Protein Variants with Significantly Improved Quantum Yield. *J Agric Food Chem* **68**, 5873-5879, doi:10.1021/acs.jafc.0c00121 (2020).

53 Chia, H. E., Marsh, E. N. G. & Biteen, J. S. Extending fluorescence microscopy into anaerobic environments. *Curr Opin Chem Biol* **51**, 98-104, doi:10.1016/j.cbpa.2019.05.008 (2019).

54 Chia, H. E., Zuo, T., Koropatkin, N. M., Marsh, E. N. G. & Biteen, J. S. Imaging living obligate anaerobic bacteria with bilin-binding fluorescent proteins. *Curr Res Microb Sci* **1**, 1-6, doi:10.1016/j.crmicr.2020.04.001 (2020).

55 Turner, L., Ping, L., Neubauer, M. & Berg, H. C. Visualizing Flagella while Tracking Bacteria. *Biophysical Journal* **111**, 630-639, doi:10.1016/j.bpj.2016.05.053 (2016).

56 Kuhn, M. J. *et al.* Spatial arrangement of several flagellins within bacterial flagella improves motility in different environments. *Nat Commun* **9**, 5369, doi:10.1038/s41467-018-07802-w (2018).

57 Bernas, T., Zarebski, M., Dobrucki, J. W. & Cook, P. R. Minimizing photobleaching during confocal microscopy of fluorescent probes bound to chromatin: role of anoxia and photon flux. *J Microsc* **215**, 281-296, doi:10.1111/j.0022-2720.2004.01377.x (2004).

58 Boudreau, C. *et al.* Excitation Light Dose Engineering to Reduce Photo-bleaching and Photo-toxicity. *Sci Rep* **6**, 30892, doi:10.1038/srep30892 (2016).

59 Giloh, H. & Sedat, J. W. Fluorescence microscopy: reduced photobleaching of rhodamine and fluorescein protein conjugates by n-propyl gallate. *Science* **217**, 1252-1255, doi:10.1126/science.7112126 (1982).

60 Schindelin, J. *et al.* Fiji: an open-source platform for biological-image analysis. *Nature methods* **9**, 676-682, doi:10.1038/nmeth.2019 (2012).

61 Sirico, D. G. *et al.* Compensation of aberrations in holographic microscopes: main strategies and applications. *Applied Physics B* **128**, 78, doi:10.1007/s00340-022-07798-8 (2022).

62 Sage, D. *et al.* DeconvolutionLab2: An open-source software for deconvolution microscopy. *Methods* **115**, 28-41, doi:10.1016/j.ymeth.2016.12.015 (2017).

63 Jeckel, H. & Drescher, K. Advances and opportunities in image analysis of bacterial cells and communities. *FEMS Microbiol Rev* **45**, doi:10.1093/femsre/fuaa062 (2021).

64 Berg, H. C. & Brown, D. A. Chemotaxis in Escherichia coli analysed by three-dimensional tracking. *Nature* **239**, 500-504, doi:10.1038/239500a0 (1972).

65 Schneider, W. R. & Doetsch, R. N. Velocity measurements of motile bacteria by use of a videotape recording technique. *Appl Microbiol* **27**, 283-284, doi:10.1128/am.27.1.283-284.1974 (1974).

66 Tinevez, J. Y. *et al.* TrackMate: An open and extensible platform for single-particle tracking. *Methods* **115**, 80-90, doi:10.1016/j.ymeth.2016.09.016 (2017).

67 Ershov, D. *et al.* TrackMate 7: integrating state-of-the-art segmentation algorithms into tracking pipelines. *Nat Methods* **19**, 829-832, doi:10.1038/s41592-022-01507-1 (2022).

68 O'Connor, O. M., Alnahhas, R. N., Lugagne, J. B. & Dunlop, M. J. DeLTA 2.0: A deep learning pipeline for quantifying single-cell spatial and temporal dynamics. *PLoS Comput Biol* **18**, e1009797, doi:10.1371/journal.pcbi.1009797 (2022).

69 Deter, H. S., Dies, M., Cameron, C. C., Butzin, N. C. & Buceta, J. A Cell Segmentation/Tracking Tool Based on Machine Learning. *Methods Mol Biol* **2040**, 399-422, doi:10.1007/978-1-4939-9686-5_19 (2019).

70 Newby, J. M., Schaefer, A. M., Lee, P. T., Forest, M. G. & Lai, S. K. Convolutional neural networks automate detection for tracking of submicron-scale particles in 2D and 3D. *Proc Natl Acad Sci U S A* **115**, 9026-9031, doi:10.1073/pnas.1804420115 (2018).

71 Meacock, O. J. & Durham, W. M. Tracking bacteria at high density with FAST, the Feature-Assisted Segmenter/Tracker. *bioRxiv*, 2021.2011.2026.470050, doi:10.1101/2021.11.26.470050 (2021).

72 Xie, J., Khan, S. & Shah, M. in *Medical Image Computing and Computer-Assisted Intervention – MICCAI 2008.* (eds Dimitris Metaxas, Leon Axel, Gabor Fichtinger, & Gábor Székely) 824-832 (Springer Berlin Heidelberg).

73 Martinez, V. A. *et al.* Differential dynamic microscopy: a high-throughput method for characterizing the motility of microorganisms. *Biophys J* **103**, 1637-1647, doi:10.1016/j.bpj.2012.08.045 (2012).

74 Wilson, L. G. *et al.* Differential dynamic microscopy of bacterial motility. *Phys Rev Lett* **106**, 018101, doi:10.1103/PhysRevLett.106.018101 (2011).

75 Stocker, R. Reverse and flick: Hybrid locomotion in bacteria. *Proc Natl Acad Sci U S A* **108**, 2635-2636, doi:10.1073/pnas.1019199108 (2011).

76 Rosser, G. *et al.* Novel methods for analysing bacterial tracks reveal persistence in Rhodobacter sphaeroides. *PLoS Comput Biol* **9**, e1003276, doi:10.1371/journal.pcbi.1003276 (2013).

Chapter 3: Quantification of Motility of *Bacillus subtilis* at Temperatures up to 84C Using a Submersible Volumetric Microscope and Automated Tracking

The work described in this chapter was published in the Extreme Microbiology section of *Frontiers in Microbiology* on April 21, 2022. It is the result of work by Megan M. Dubay, Nikki Johnston, Jake Lee, Mark Wronkiewicz, Christian Lindensmith, and Jay Nadeau. Work described within was completed, in part, at Jet Propulsion Laboratory, California Institute of Technology and under contract with the National Aeronautics and Space Administration.

Citation: Dubay MM, Johnston N, Wronkiewicz M, Lee J, Lindensmith CA and Nadeau JL (2022) Quantification of Motility in Bacillus subtilis at Temperatures Up to 84°C Using a Submersible Volumetric Microscope and Automated Tracking. *Front. Microbiol.* 13:836808. doi: 10.3389/fmicb.2022.836808

Here we discuss the development of a system for studying motility in environments up to 100C. This system design is useful for thermophilic archaea such as *P. furiosus,* which live in environments with temperatures exceeding 85C. In addition to studying thermophilic species, it is also useful for studying motility changes in response to changing environmental temperature. As a proof of concept for this design, we examined samples of *B. subtilis*, which is incubated at 30C and exists at room temperature environments, as the environment increased in temperature. *B. subtilis* is already known to have genes that control stress responses, including heat stresses. The HELM software developed at JPL was used to quantify the changes in motility observed.

Author Contributions

MD: construction and calibration of thermal control apparatus; growth and maintenance of bacteria; data collection; data analysis; figure creation; data archiving; writing; development of supplemental materials. NJ: construction and calibration of thermal control apparatus; growth and maintenance of bacteria; data collection; data analysis; figure creation; data archiving; writing. MW and JL: Development of HELM tracking software; troubleshooting and debugging of software and addition of new features upon request. CL: original concept design; acquisition of funding. JN: acquisition of funding; supervision and planning of experiments; data analysis; writing. All authors: editing and approval of final draft.

Quantification of motility in *Bacillus subtilis* at temperatures up to 84 ºC using a submersible volumetric microscope and automated tracking

Megan M. Dubay[1], Nikki Johnston[1], Mark Wronkiewicz[2], Jake Lee[2], Christian A. Lindensmith[2] and Jay L. Nadeau[1]

[1]Portland State University, Department of Physics, 1719 SW 10th Ave, Portland OR 97201, [2]Jet Propulsion Laboratory, California Institute of Technology, 4800 Oak Grove Dr., Pasadena, CA 91109

Abstract

We describe a system for high-temperature investigations of bacterial motility using a digital holographic microscope completely submerged in heated water. Temperatures above 90 ºC could be achieved, with a constant 5 ºC offset between the sample temperature and the surrounding water bath. Using this system, we observed active motility in *Bacillus subtilis* up to 66 ºC. As temperatures rose, most cells became immobilized on the surface, but a fraction of cells remained highly motile at distances of > 100 µm above the surface. Suspended non-motile cells showed Brownian motion that scaled consistently with temperature and viscosity. A novel open-source automated tracking package was used to obtain 2D tracks of motile cells and quantify motility parameters, showing that swimming speed increased with temperature until ~40 ºC, then plateaued. These findings are consistent with the observed heterogeneity of *B. subtilis* populations, and represent the highest reported temperature for swimming in this species. This technique is a simple, low-cost method for quantifying motility at high temperatures and could be useful for investigation of many different cell types, including thermophilic archaea.

1 Introduction

The effects of elevated temperatures on bacterial motility have not been fully explored. There are both physical and physiological effects of temperature on flagellar swimming at low Reynolds number. Both viscosity and temperature contribute to the Stokes-Einstein equation for the diffusion coefficient, D

$$D = \frac{k_B T}{6\pi\eta r} \quad (1)$$

where k_B is Boltzmann's constant, T is the absolute temperature, η is the dynamic viscosity of the medium, and r is the radius of the diffusing particle. Water shows a dramatic decrease in dynamic viscosity with temperature, described by the equation

$$\eta(T) = Ae^{B/(T-C)} \text{ (2),}$$

where A= 2.414 x 10^{-5} Pa•s, B=247.8 K, and C=140 K. This results in values ranging from 1.002 mPa s at 20 ºC to 0.315 mPa s at 90 ºC. As a result, there is a significant change in the rate of Brownian motion of cells at elevated temperatures: as a simple example, 0.30 $\mu m^2/s$ at 33 ºC for a 1 µm diameter cell, and 0.86 $\mu m^2/s$ for the same cell at 91 ºC.

The effects of viscosity on active swimming are less clear. The drag force is proportional to η and thus it would be expected that swimming speeds would increase with decreased viscosity, but instead a surprising decrease in bacterial swimming speeds with decreased viscosity is seen in polymer solutions. Several papers have suggested that this is due to microstructure of the polymer (Zottl and Yeomans, 2019) (Magariyama and Kudo, 2002). In ordinary aqueous solution, a roughly linear increase in swimming speed with temperatures up to 50 ºC has been reported for *Escherichia coli* (Maeda et al., 1976) and for multiple other strains representing polar, bipolar, and peritrichous flagellar arrangements (Schneider and Doetsch, 1977). One study reported a linear increase in *E. coli* swimming speed with temperature up to 40 ºC in medium supplemented with L-serine; in the absence of supplementation, speeds increased only up to 30 ºC and decreased thereafter (Demir and Salman, 2012). This linear relationship is related to increased flagellar rotation rates at high temperatures as well as altered viscosities both inside and outside the cell and has been modeled semi-empirically using a large number of available motility datasets. Speed is generally assumed to be directly proportional to flagellar rotation rate; though this is not true in all datasets, a positive correlation is always present (Humphries, 2013).

As a simple model, the force on a swimming cell may be approximated as the sum of the flagellar force *F* and the velocity-dependent drag force *Dv*,

$$F = ma = F - Dv \quad (3),$$

where D is the drag coefficient given in Eq. (1). Although models predict a viscosity dependence, recent studies have found that F is independent of viscosity (Armstrong et al., 2020). This equation of motion yields a terminal velocity of

$$v_\infty = \frac{F}{D} \propto \frac{F}{\eta}, \ (4)$$

where the terminal velocity should be observed during a long run once the cell is no longer accelerating. The time-averaged velocity over a long run should thus approximate v_∞.

None of these models take into account the upper limits of possible motility of different strains resulting from protein denaturation or general organism stress.

Microorganisms show complex heat shock responses, and the expression and maintenance of flagella can be affected by genes related to heat stress. Motility is a complex phenotype under tight regulation in all microorganisms that express it. *Bacillus subtilis* is a model organism for which regulation of motility genes (Mukherjee and Kearns, 2014) and heat shock responses (Schumann, 2003) have been well studied. There is a strict dependence upon FlgN for motility in this species (Cairns et al., 2014). Flagellar synthesis is affected by a number of the genes involved in the heat shock response. As temperature increases, proteins denature, and protein degradation systems clear the damaged proteins. The ClpCP complex in *Bacillus subtilis* degrades stress-damaged proteins as well as taking part in regulatory degradation. It also influences motility by both direct and indirect mechanisms. The absence of Clp proteases results in defective motility, likely due to accumulation of Spx, which suppresses flagellar gene expression. Cells under stress do not necessarily lose motility immediately via this mechanism, since existing flagella are not affected, rather the production of new flagella (Moliere et al., 2016).

The heat shock responses of *B. subtilis* allow it to grow to at least 53 ºC (Warth, 1978). Much has been written about the mechanisms of thermotolerance in this species. The sigma factor σ^B provides non-specific stress resistance, which includes thermotolerance. Its activation induces the expression of ~200 target genes (Nannapaneni et al., 2012) (Hecker et al., 1996) (Young et al., 2013). Cells do not need to be exposed to heat stress in order to gain thermotolerance via this mechanism. In addition, there are specific heat-shock responses that turn on under conditions of mild heat stress, leading to protection from otherwise lethal temperatures. At least three classes of genes are heat-shock inducible.

Because of the complexity of both the heat shock response and regulation of motility genes, it is difficult to predict the effects of high temperature on swimming motility. Most studies focus on growth rather than persistence of swimming. The persistence of the motility phenotype under conditions of heat stress has been little explored, largely due to technical difficulties of imaging and image analysis as temperatures rise. One study reported that convection currents made tracking difficult above 40 ºC (Riekeles et al., 2021). In addition, most heated stages can only achieve temperatures of 55-60 ºC. We hypothesized here that some fraction of *B. subtilis* cells would be capable of active motility at temperatures above the maximum growth temperature, with significant variations consistent with the highly heterogeneous responses of this species to stress (Syvertsson et al., 2021b) (Kearns and Losick, 2005;Lopez et al., 2009).

A few studies have reported microscopic imaging systems able to reach temperatures up to the boiling point of water, but none fit our precise goals. A 1995 study of *Thermotoga maritima* used a capillary between two Peltier elements(Gluch et al., 1995). A more recent study reported an environmental chamber for microbial imaging that allows for pressure and temperature control(Nishiyama and Arai, 2017). For studying hyperthermophilic archaea, a "Sulfoscope" with a heated cap and stage was recently described where temperatures of 75 ºC were stably maintained; temperatures up to 90 ºC were achieved but led to significant evaporation(Pulschen et al., 2020). This design is appropriate for fluorescence microscopy and is especially valuable for imaging immobilized cells, a technique which was described in detail in the study using a semi-soft Gelrite pad. Air objectives were used. Another recent study attained higher resolution using oil-immersion objectives heated to 65 ºC, with the entire chamber heated to 75 ºC. Imaging was by differential interference contrast (DIC) (Charles-Orszag et al., 2021).

While high resolution is sometimes desirable, our goal was to create a simple, inexpensive system for imaging at high temperatures with a particular focus on tracking of microorganisms in a large volume of view. Thus, the goal was to maximize the depth of field with sufficient resolution to distinguish individual cells, but not subcellular structure. We use a custom holographic microscope entirely submerged in a heated water bath in order to examine motility at temperatures between 28 and 85 ºC, with capability of temperatures up to at least 95 ºC. The materials for the heated bath are inexpensive (<$200 USD in 2022) and a complete parts list is included for both the microscope and bath, with a total cost of <$7000 USD for the complete system. Because the system was designed for field use and no compound objective lenses are used, there are minimal effects of temperature on the instrument, even up to the boiling point.

With this system, cultures of *B. subtilis* were either heated slowly over a period of 4 hours or exposed rapidly by submersion into a pre-heated bath. Individual cells were tracked, and velocities, accelerations, turn frequency, and correlation functions were all quantified using a custom open-source autonomous program. The program successfully controlled for thermal currents, classifying tracks into "motile" vs. "non-motile" based upon a defined algorithm. All active tracks were manually confirmed to correspond to cells. Active swimming was observed up to 66 ºC in some fraction of the cells; increasing numbers of immobile cells collected on the sample chamber surface as temperatures increased. Cells up to 90 ºC remained normal in morphology, without signs of sporulation. Dead cells showed little movement until temperatures >60 ºC, at which point convection currents became appreciable; however, these were readily distinguished from active motility by inspection as well as automated tracking tools. These techniques will be of interest to anyone exploring bacterial behavior at temperatures up to the boiling point of water.

2 Materials and Methods

2.1 Microscope and Temperature Control

The microscope used in this study was a common-path off-axis digital holographic microscope (DHM) as described previously (Wallace et al., 2015) (U.S. Patent US20160131882A1) **(Figure 1A)**. Briefly, a single-mode laser (520 nm, Thorlabs, Newton, NJ) was collimated and passed through separate reference and sample channels held in a single plane to prevent mis-alignment. The objective lenses were simple achromats (numerical aperture 0.31, part number 47-689-INK, Edmund Optics, Barrington, NJ), yielding an effective magnification of ~20x and XY spatial resolution of ~1.0 µm. Since focusing is performed numerically with DHM, the sample stage was fixed in position with the in-focus plane Z=0 at approximately the center of the sample chamber. The camera was a Prosilica 2460GT (Allied Vision, purchased from Edmund Optics) monochrome camera with a 5 MPixel, 3.45 µm pixel pitch format and 15 frames/s maximum frame rate, with acquisition windowed to 2048x2048 px. A higher frame rate (23.7 fps) can be achieved by substituting the newer Prosilica 2560GT without further modification of the system. Both recommended cameras use global shutter detector readout; rolling shutter readout cameras are not recommended unless careful consideration is taken in avoiding distortion of fringes during readout.

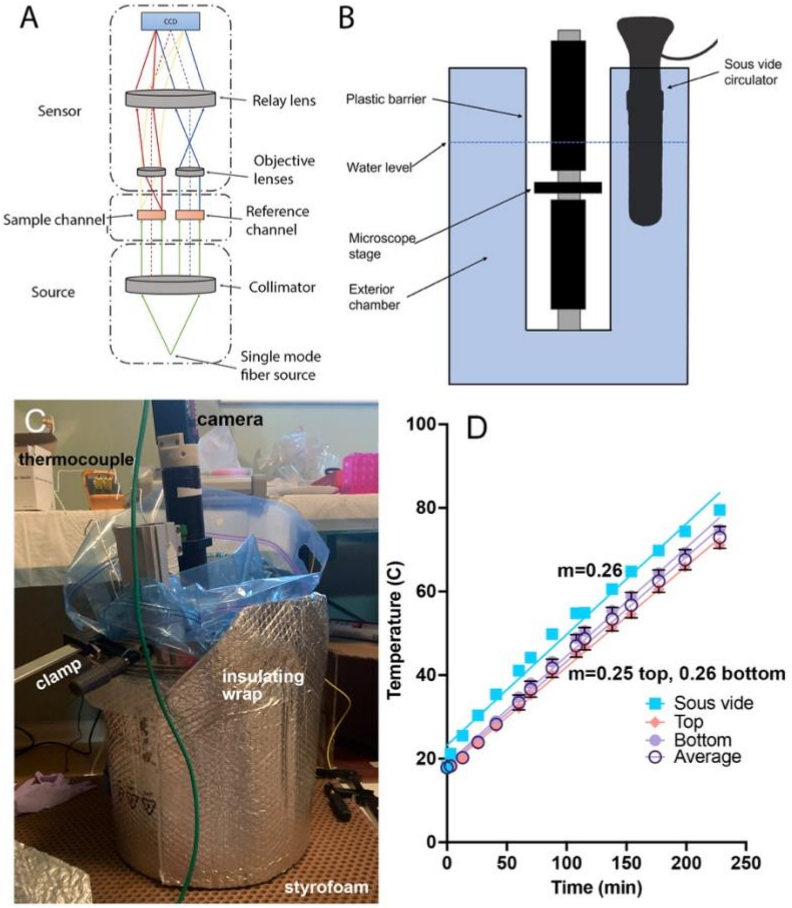

Figure 1. Temperature-controlled microscope setup. (A) Schematic of off-axis DHM used in these experiments. (B) The microscope was protected by a heavy-duty plastic bag and submerged in heated water to control the sample temperature. (C) Photograph of the complete setup showing the insulating materials necessary to attain the highest temperatures. The microscope is submerged into the pot with the sample chamber located several cm below the water surface. The insulation shown is required for achieving water and sample temperatures above ~70 ºC. (D) Correspondence between the sous vide measured water temperature (verified with a laboratory thermometer) and thermocouple measurements of the sample chamber at top and bottom, along with the average between top and bottom. The slope of the temperature change was consistent between the bath and the chamber, with a nearly constant offset of 5 ºC. The lines are linear fits with slopes indicated.

To control the temperature of the sample chamber, the entire microscope was placed into a stainless steel cooking pot (36 quart, Bayou Classic, sold through amazon.com) and protected by a 5-gallon, 4 mil thickness plastic bag (Ziploc brand or autoclave bag). The laser was kept out of the bath and coupled to the microscope through its single-mode fiber output. The camera was kept above the water level of the bath by the microscope tube. The pot was filled with water to a level above the top of the sample chamber, and the temperature of the water was gradually increased at a constant rate of 4.3 ºC/min using a sous vide circulator (Monoprice Model#: 121594, 800W, 4 gallon capacity) (**Figure 1 B, C**). The water temperature indicated on the circulator was confirmed using a laboratory thermometer (Fisherbrand). In order to raise the temperature above ~80 ºC, it was necessary to insulate the pot with metallized bubble wrap (**Figure 1C**). A thermocouple (Gain Express K-Type, sold through amazon.com) was taped both above and below the chamber, in direct contact with the chamber, in an independent set of experiments to determine how the sample temperature corresponded to the water temperature; a nearly constant offset of 5 ºC was seen between the chamber and the water temperature, and this correction was applied to all reported chamber temperatures (**Figure 1D**). **Supplementary Methods** with **Supplementary Figures S1-S2** show the steps involved in setup, and **Supplementary Datasheet 1** provides a parts list for the entire instrument with purchasing links. The costliest elements are the laser and camera.

Preliminary thermal testing of elements was performed by submerging individual parts of the setup into water in Ziploc bags and heating the water using the sous vide controller to its maximum temperature (just below boiling). In the case of the objective lens holder, because of its small size and low cost, it was placed into boiling water on the stovetop both with and without the lenses installed. The upper temperature limit of the microscope is set by the plastic used in the 3D-printed lens holder and the bonding of the sample chamber; substitutions of these components with higher temperature materials would enable higher temperature investigations. None of the components was tested above 100 ºC in this study.

2.2 Samples and chambers

Bacillus subtilis type strain (ATCC 6051) was obtained from the American Type Culture Collection, Manassas, VA. Stocks were maintained at -80 ºC and periodically streaked onto lysogeny broth (LB, Fisher Scientific, Pittsburgh, PA)-agar plates. 16-24 hours before each experiment, single colonies were picked from plates, seeded into liquid LB, and incubated at 30 ºC with shaking to mid-log phase (OD ~0.6 as measured on a Clariostar plate reader). After incubation, samples were diluted 1:1000-1:100 into motility medium (10 mM phosphate buffer pH 7.4, 10 mM NaCl, 0.1 mM EDTA) and moved to custom sample chambers at 20 ± 2 ºC. To control for any possible non-biological motion at high temperatures, an additional set of experiments was performed using heat-killed *B. subtilis* cells at the same concentration. The cells were exposed to boiling water for 30 min, then pelleted and washed twice with motility medium before imaging.

The sample chambers (product of Aline, Rancho Dominguez, CA) are composed of two channels, one for the sample and one as a reference channel which is filled with 0.9%

saline solution or sterile growth medium (**Figure 2**). These are composed of two layers of optical quality glass with a middle acrylic layer forming the channels. Homemade chambers using microscope slides, coverslips, and adhesive material such as silicone or Teflon may also be used; for detailed instructions, see **Supplementary Methods** with **Supplementary Figures S3-S5**. The depth of the chamber is 1.0 mm, which allows for motility far away from the surfaces in order to eliminate surface influences on motility (Li et al., 2008;Giacche et al., 2010;Li et al., 2011). The sample was placed into the microscope before immersion and left throughout the duration of the heating. Replicate experiments (2-4) were performed on different days with independent *B. subtilis* cultures in order to confirm the reproducibility of the results. Cell density in the chambers varied from ~10^5-10^6 cells/mL.

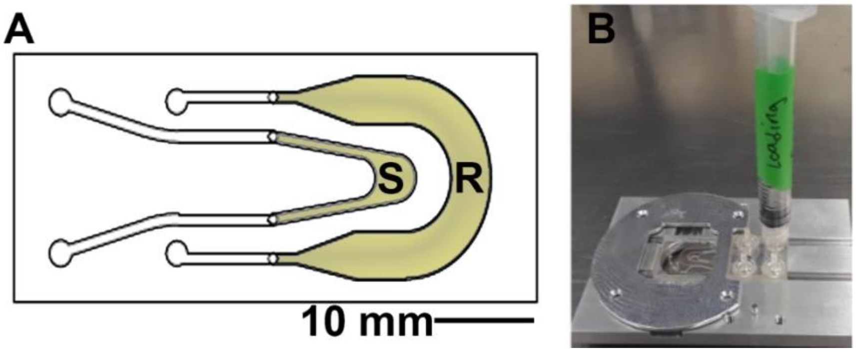

Figure 2. Sample chamber arrangement. (A) Schematic of the 1 mm deep chamber, showing the sample (S) and reference (R) channels that permit the off-axis DHM geometry. The volume of view of each snapshot is 365 μm x 365 μm x 1 mm in x, y, and z. (B) The chambers were loaded using a 1 mL syringe and placed onto the microscope stage at a fixed focus before immersion.

2.3 Acquisition and reconstruction of holograms

Data were acquired using a custom, open-source software package, DHMx (https://github.com/dhm-org/dhm_suite). Recordings were between 30 and 60 seconds long, with a maximum frame rate of 15 frames per second (fps). Recordings were obtained every ~5°C until reaching a maximum sample temperature of 84°C. Additional tests were performed which subjected the bacteria to rapid increases in temperature. Samples were loaded into chambers at 20°C and submerged into pre-heated water at varying temperatures. For these "heat shock" experiments, recordings were obtained immediately after submersion as well as 2 and 10 minutes afterwards. The 10 minute datasets were chosen for analysis.

The holograms for each recording were either median subtracted (as we described previously (Bedrossian et al., 2020)) or frame-to-frame subtracted then reconstructed in amplitude using Fiji (ImageJ)(RRID:SCR_002285) (Schindelin et al., 2012). Reconstructions were performed using the angular spectrum method (Mann et al., 2005) implemented in a custom plug-in described in detail elsewhere (Cohoe et al., 2019) and available from our update site (https://github.com/sudgy/). The choice of frame-to-frame subtraction was necessary at temperatures > 50 ºC in order to eliminate noise due to nonstationary cells on the chamber surface. The z thickness chosen for reconstruction ranged from 400-800 μm and varied somewhat among datasets depending upon the location of active cells. The resulting stacks were maximum projected in Z using Fiji to create a 2D time series of all of the cells of interest.

2.4 High resolution light and fluorescence microscopy

In order to carefully evaluate cell morphology and possible presence of spores, cells were examined on an Olympus IX-71 inverted microscope with a 100x, NA=1.4 oil immersion objective using either brightfield illumination or fluorescence illumination with a Hg lamp and a 450/50 nm excitation filter and 520 nm longpass (Chroma Technology, Bellows Falls, VT).

2.5 Fraction motile

Non-motile cells were difficult to count from images, especially at higher temperatures as cells began to cluster, so the fraction of motile cells was estimated as the number of motile cells per volume of view averaged over the length of the recording, divided by the total cell concentration (as measured by original OD divided by dilution factor; the relationship between OD and cell concentration was established using a hemocytometer). The instantaneous volume of view is 0.365 x 0.365 x1 mm^3, or 0.13 µL, corresponding to ~100 cells/frame at 10^6 cells/mL. The number of motile cells per frame was calculated using frame-to-frame subtracted projections so that non-motile cells did not interfere with the analysis. Fiji Analyze Particles (https://imagej.net/imaging/particle-analysis) was used to count the number of cells per frame.

2.6 Tracking and statistics

Bacteria were tracked using a custom software package, Holographic Examination for Life-like Motility (HELM) (https://github.com/JPLMLIA/OWLS-Autonomy), which was developed to autonomously detect, track, and characterize motile cells. HELM identifies pixel changes in sequential DHM images, tracks clusters of change as particle movement, and classifies particles as motile or non-motile based on their movement patterns. The pixel changes are computed by simple background subtraction of the median video image. Clusters of pixel changes are identified using DBSCAN. Tracks are then generated using the Linear Assignment Problem (LAP) tracker method (Jaqaman et al., 2008). With the spatiotemporal points, HELM computes approximately two dozen metrics that form a feature vector for each track. These include features like mean speed, mean turn angle, total track displacement, etc. A random forest classifier (Breiman, 2001) is then used to classify each track as motile or non-motile. The classifier was trained using manually labeled tracks from both prepared laboratory and field-acquired ocean water samples, both with and without fluid flow in the sample chamber. HELM can be used on raw, unreconstructed holograms or on 2D projections of reconstructed holograms. Analysis presented here was performed on projections of reconstructed holograms as described in Section 3.3.

HELM also generates multiple contextual products to support assessment of a DHM recording. One of these, the Motion History Image (MHI), summarizes a full video in one image by color mapping each pixel to the time index of largest intensity change. The MHI image allows a rapid understanding of how many particles were present in the recording as well as the presence and characteristics of potential motile organisms. Diffusion coefficients were measured using NanoTrackJ (Wagner et al., 2014). A video of at least 30 s containing at least 10 trackable particles was analyzed using the Maxima & Gaussian Fit center estimator and the covariance diffusion coefficient estimator. Parameters used were: minimum estimated particle size, 20 pixels; minimum number of steps per track, 5; pixel size, 178 nm; and frame rate 15 frames/s.

Statistical analysis of HELM outputs and graphing were performed using Prism 9 (GraphPad Software, San Diego, CA). Statistical relevance was estimated using the

ANOVA package in Prism after ensuring that distributions were Gaussian. The correlation matrix was computed using the Multivariable Analysis package in Prism.

3 Results

3.1 Microscope function and maintenance at high temperatures

We tested all elements of the system for their ability to withstand temperatures up to 100 ºC. The DHM optics are robust, as they contain no compound objectives, adhesives, or other heat-sensitive elements. The 3D printed lens holder and objectives withstood boiling up to 30 minutes. The most sensitive element of the setup was the fiber optic cable. Under preliminary tests, the cable housing degraded, allowing light to escape, when the cable was heated to 90 ºC. This could be prevented by shielding the cable from the heat using an aluminum mini-box as shown in **Supplementary Figure S1.** On occasion, condensation would form on the sample chamber, objective lens, or collimating lens. This could be removed by wiping with lens paper. After multiple rounds of experiments or if image quality appeared poor, all of the lenses were removed and cleaned with 100% isopropanol. It was also important to keep the camera outside of the hot area to prevent condensation on the window.

3.2 Morphology and Brownian motion

There was no significant difference in size or overall morphology of motile cells as the temperature increased (**Fig. 3, Figure 4 A**). Non-motile cells showed increased rates of Brownian motion consistent with scaling of diffusion rates with temperature ($k_B T$) and dynamic viscosity of water (η). The Stokes-Einstein relation (Eq. 1) gave an excellent fit to the measured data for particle radius r=2.1 µm (**Fig. 4 B**). This was consistent with the sizes measured by direct imaging, with a large amount of variability seen in both measured size and diffusion coefficient due to the presence of elongated and clustered cells. For temperatures higher than 44 ºC, Brownian motion was impossible to evaluate because of either thermal currents or large numbers of cells immobilized on the glass surface.

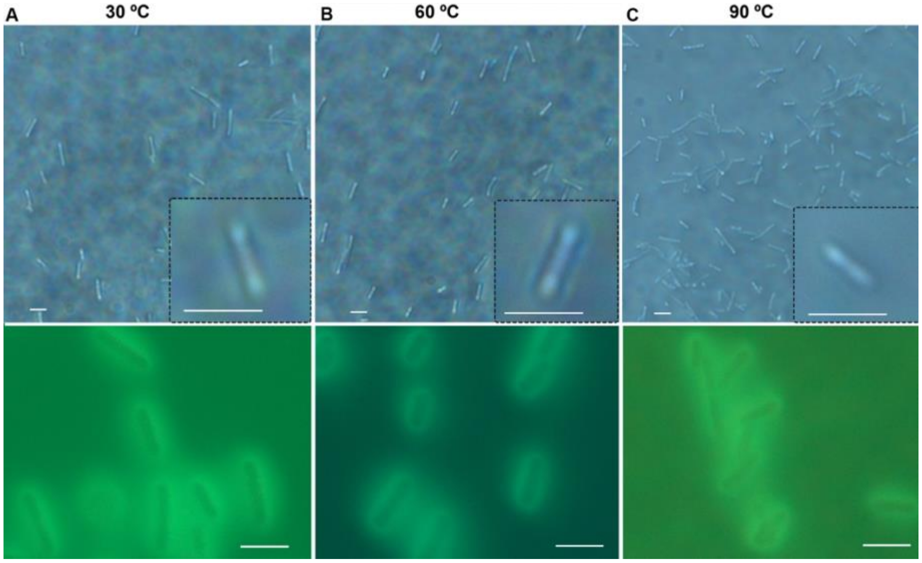

Figure 3. Morphology of cells. General appearance and size of *B. subtilis* at normal and elevated temperatures. Shown are phase contrast (top row) and autofluorescence (bottom row); scale bar= 5 µm. (a) 30 ºC. (b) 60 ºC. (c) 90 ºC.

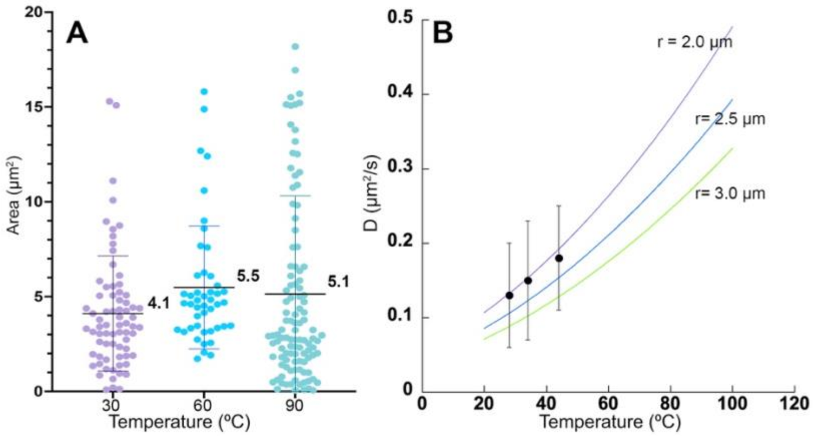

Figure 4. Cell sizes and diffusion coefficients with temperature. (A) Cell area as estimated by microscopy, shown as mean ± standard deviation. The differences in the means from one temperature

to the next was not significant. (B) Measured diffusion coefficients at 3 temperatures (black dots), with measured standard deviations, compared with predicted values according to Eq. (1) for particle radii of 2.0, 2.5, and 3.0 µm.

3.3 Motility analysis

Motility analysis was performed on reconstructions and projections of holograms. An example hologram is shown in **Fig. 5A**, and a single-plane amplitude reconstruction in **Fig. 5B**. Single plane reconstructions provided qualitative insight into cell morphologies, speeds, and fraction of motile cells; however, their signal to noise ratio was insufficient for automated tracking. Maximum projections through 40-80 Z planes, representing 400-800 µm sample depth (**Fig. 5C**), permitted automated tracking to create 2D trajectories. Motion history images (MHIs, as described in Methods) were used to identify tracks of motile organisms from these projections (see **Supplementary Video 1). Figure 6** shows time-coded MHIs for temperatures from 28 to 84 ºC for a selected set of experiments. The spacing between points on each track gives a rough estimate of cell speed. Where thermal drift was significant, motile cells could be identified by their paths of travel against the drift current. Only cells moving counter to the thermal drift were selected for tracking, as they clearly represented active motility.

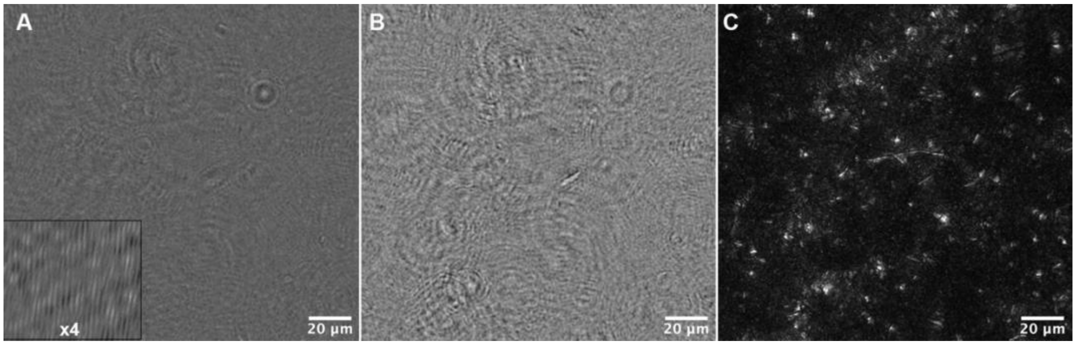

Figure 5. Data reconstruction and processing for tracking. (A) A portion of the field of view of a median-subtracted hologram from the 34 ºC dataset. The inset shows part of the image magnified 4x

to show the fringes. (B) Amplitude reconstruction of the same field of view in (A) at +50 µm. (C) Maximum Z projection of the same field of view, representing reconstructions from -200 to +200 µm in steps of 10 µm.

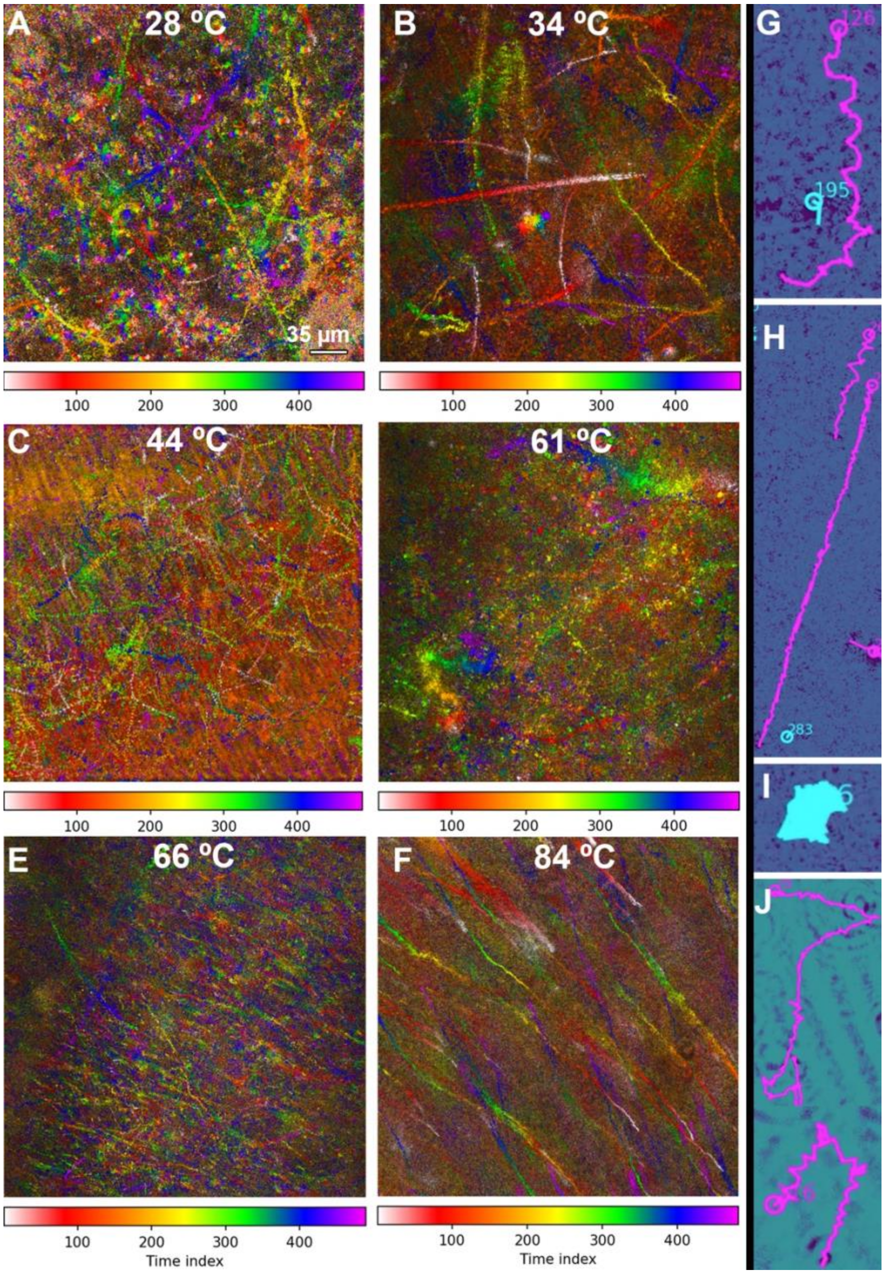

Figure 6. MHI analysis shows changes in motility patterns with increasing temperature and assists in identifying motile tracks. The tracks are time-coded, with the time index indicating frame number (15 frames/s). The scale bar applies to all panels. (A-F) Full field of view of all identified tracks in selected datasets. (A) 28 ºC, showing a distribution of motile and non-motile cells and distinct swimming patterns. (B) 34 ºC, showing increased motility and speed. (c) 44 ºC, showing nearly all cells motile at high speed. (D) 61 ºC, showing a reduction in the number of motile cells, but some

swimming at high speed. (E) 66 ºC, showing a large amount of thermal drift with a few motile cells. (F) 84 ºC, with all motion due to thermal drift. (G-J) selected examples of swimming types identified in the tracks. Magenta indicates tracks identified as motile by the software; tracks in cyan were identified as non-motile. (G) Helical swimming. (H) Long straight runs. (I) Circling or spinning. (J) Run and tumble.

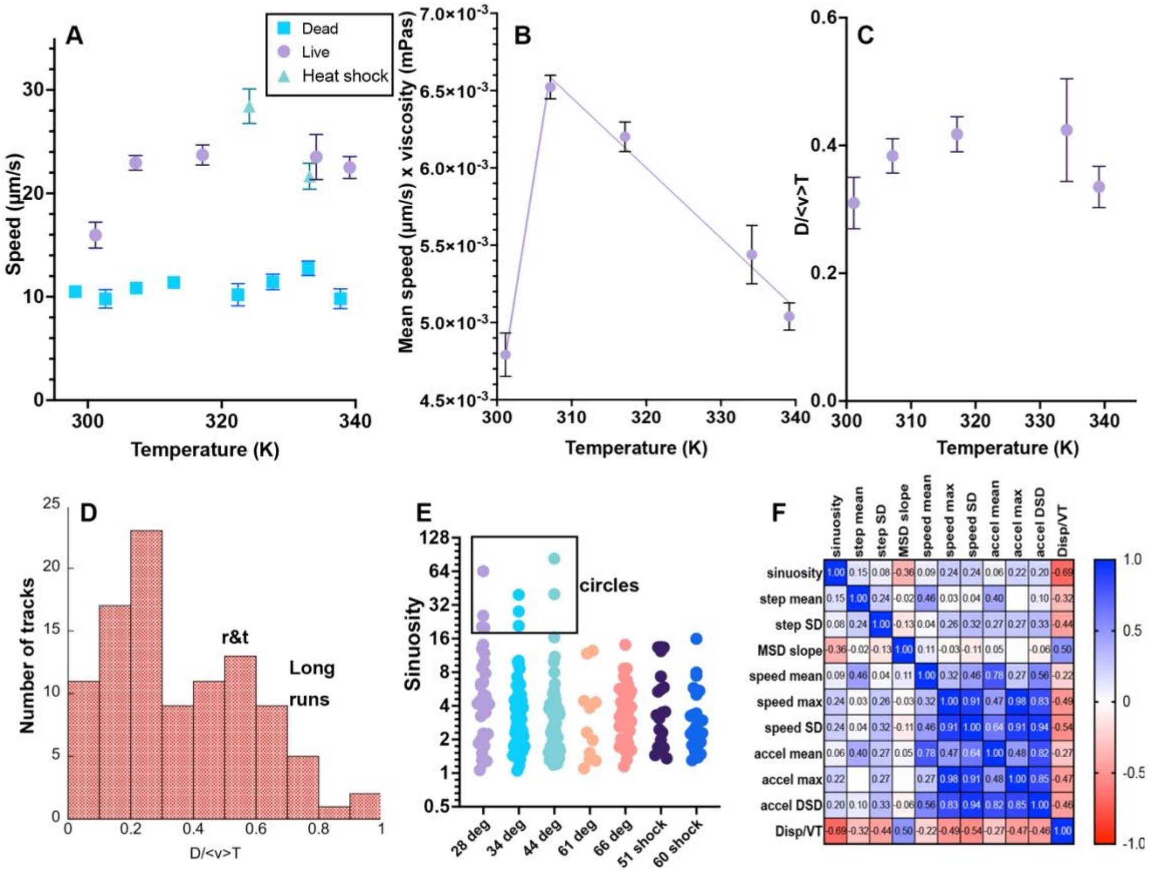

	sinuosity	step mean	step SD	MSD slope	speed mean	speed max	speed SD	accel mean	accel max	accel DSD	Disp/VT
sinuosity	1.00	0.15	0.08	-0.36	0.09	0.24	0.24	0.06	0.22	0.20	-0.69
step mean	0.15	1.00	0.24	-0.02	0.46	0.03	0.04	0.40		0.10	-0.32
step SD	0.08	0.24	1.00	-0.13	0.04	0.26	0.32	0.27	0.27	0.33	-0.44
MSD slope	-0.36	-0.02	-0.13	1.00	0.11	-0.03	-0.11	0.05		-0.06	0.50
speed mean	0.09	0.46	0.04	0.11	1.00	0.32	0.46	0.78	0.27	0.56	-0.22
speed max	0.24	0.03	0.26	-0.03	0.32	1.00	0.91	0.47	0.98	0.83	-0.49
speed SD	0.24	0.04	0.32	-0.11	0.46	0.91	1.00	0.64	0.91	0.94	-0.54
accel mean	0.06	0.40	0.27	0.05	0.78	0.47	0.64	1.00	0.48	0.82	-0.27
accel max	0.22		0.27		0.27	0.98	0.91	0.48	1.00	0.85	-0.47
accel DSD	0.20	0.10	0.33	-0.06	0.56	0.83	0.94	0.82	0.85	1.00	-0.46
Disp/VT	-0.69	-0.32	-0.44	0.50	-0.22	-0.49	-0.54	-0.27	-0.47	-0.46	1.00

Figure 7. Selected motility parameters. Definitions of the parameters, values and statistical significance are given in the text. Error bars shown are mean ± standard error of the mean unless noted. Numbers of analyzed tracks and their classifications are given in **Table 1**. When error bars do not appear, they are smaller than the symbols. (A) Mean speed. (B) Mean speed times viscosity of water at that temperature. The lines are linear fits to temperatures above or below 310 K. (C) Total displacement normalized to track length and average speed <v>. (D) Histogram of selected values of D/<v>T, showing classification into long runs vs. run-and-tumble traces. (F) Sinuosity (no error bars given as the distributions were not Gaussian and the mean value had little significance). These values are plotted on a Log_2 scale for ease of visualization of the ranges involved. Circular tracks were identified as those with sinuosity > 20. (F) Correlation matrix of the measured parameters.

The fraction of motile cells (see **Table 1** for statistics) increased from ~20% at 28 ºC (**Fig. 6A, Supplementary Video 2**) to 25% at 34 ºC (**Fig. 6 B; Supplementary Video 3**) to >60% 44 ºC (**Fig. 6 C; Supplementary Video 4**). However, at 61 ºC and 66 ºC, the fraction of motile cells was greatly reduced, to <6% and <1%, respectively. Motile tracks could still be identified in single-plane reconstructions (**Supplementary Video 5**) and in MHI analysis projections through Z (**Fig 6 D, E, Supplementary Video 6**). At 84 ºC, only thermal currents and drift were observed, with no active counter-current motility; the fraction of motile cells was deemed 0% (**Fig. 6 F, Supplementary Video 7**). Qualitative analysis of these tracks on a cell-by-cell basis revealed that there were 4 basic track types: (1) helical tracks (**Fig. 6G**); (2) long straight runs (**Fig. 6H**); (3) circular tracks (spinning) (**Fig. 6I**); and (4) runs with tumbles and directional changes, which could feature either straight or helical swimming or some combination of both; any track with distinct directional changes was classified as run and tumble (**Fig. 6J**).

Temperature (ºC)	**Fraction of cells motile ± SD**	**Total # tracks analyzed (# replicates)**	**# fast runs/tumbles/helices/circles**	**Mean ± SD speed (µm/s) (range)**	**Mean ± SD acceleration (µm/s^2)**	**Mean ± SD displacement (µm/s) (range)**
28	20 ± 1	36 (2)	10/8/10/8	16 ± 7 (3-32)	150 ± 70	5 ± 4 (0.2-16)
34	24 ± 2	66 (2)	24/26/8/8	23 ± 6 (12-42)*	200 ± 60 *	9 ± 5 (0.7-21)
44	61 ±2*	57 (2)	18/30/5/4	24 ± 7 (8-45)*	210 ± 90 *	10 ± 6 (0.1-25)*

61	6 ± 2*	16 (2)	10/5/1/0	24 ± 7 µm/s (14-38)*	230 ± 90 *	10 ± 7 (1.3-27)
66	<1*	35 (2)	18/13/2/0	23 ± 6 (12-41)*	220 ± 70 *	8 ± 5 (1.3-26)
51 heat shock	Not done	21 (1)	2/2/10/7	28 ± 6 (15-47)*	250 ± 110 *	10 ± 7 (2-24)
60 heat shock	Not done	24 (1)	2/12/8/2	22 ± 6 (13-37)*	160 ± 70	8 ± 5 (1.1-18)

Table 1. Motility parameters. “Replicates” represent independent experiments done on different days with fresh cultures of *B. subtilis*. Tracks were characterized according to **Fig. 6** by visual inspection and correlation with parameters as in **Fig. 7**. SD=standard deviation. (*)= significantly different from value at 28 ºC (p <0.01).

Heat-killed cells showed no active motility, and the MHI images correspondingly showed few features at the lower temperatures (**Supplementary Figure S6**). Amplitude reconstructions of the holograms revealed cells undergoing slight drift and Brownian motion (**Supplementary Video 8** shows 28 ºC). At temperatures of 60 ºC and higher, substantial thermal drift and convection became apparent. At the highest temperatures, multiple drift planes could be observed, but in all cases motion was clearly due to bulk flow without any evidence of run and tumble events (**Figure S6**; **Supplementary Video 9** shows 84 ºC). HELM’s classification algorithm was 100% successful at classifying tracks as non-motile at temperatures < 50 ºC, and >95% successful at higher temperatures (**Supplementary Video 10** shows classification of tracks at 84 ºC). This classification is not based upon any one parameter, and correlating its results with physical parameters will be the subject of a future study. Visual inspection is always required to correlate tracks with cells and to perceive patterns suggesting active motility.

Quantitative analysis of tracks was performed by using the automated tracker combined with the MHI to identify tracks that represented valid cell trajectories. Tracks that were not following organisms or which were fewer than 15 frames long were excluded from analysis. **Table 1** gives classification of the analyzed motile tracks for selected datasets. Parameters extracted from these tracks are shown in **Table 1** and **Figure 7**. Data from independent experiments were consistent, so full tracking was performed using selected tracks from pools of replicates (see **Supplementary Fig. S7** for comparisons of replicate experiments). Plotted in Fig. 7 are selected parameters where significant differences were seen among the different temperatures or where parameters assisted in classifying tracks. The full datasets are available in **Supplementary Datasheets 2-7**.

The **mean speed** was defined for each trajectory as

$$\bar{v} = \frac{1}{N}\sum_{i=i}^{N} \frac{\|\vec{x}_i - \vec{x}_{i-1}\|}{\Delta t} \quad (5),$$

where N is all of the points in the identified trajectory and Δt is the (constant) frame rate. There was a significant increase in mean speed between 28ºC and all of the other elevated temperatures. There was a statistically significant difference ($p<0.001$) for comparison between 28 ºC and the other temperatures, and not significant between any other pairs. The fastest speeds were seen in the 51 ºC heat shock sample ($p< 0.001$ for comparison with 28 ºC, 35 ºC, and 60 ºC heat shock). The values for the 60 ºC heat shock were comparable to those at all other elevated temperatures (significantly different from 28 ºC and 51 ºC heat shock, all others nonsignificant). Values are given in **Table 1** and means with standard errors of the mean are plotted in **Fig. 7 A** for both live and killed cells; distributions were Gaussian at each temperature. The speeds of the killed cells were significantly less than those of the live cells, even when drift was significant. There was no significant difference in **maximum trajectory speed** seen between any pairs of data sets of live cells (not shown; means 80-100 μm/s for maximum instantaneous speeds).

The mean speed times viscosity, which should give an approximate measure of flagellar force as given in Eq. (4), decreased essentially linearly at higher temperatures. This is consistent with denaturation of the proteins as the temperatures rise, representing a typical optimum performance curve with the optimal temperature near 310 K (37 ºC) (**Fig. 7 B**). Because heat denaturation is a time-dependent process involving multiple parameters (Peterson et al., 2007), additional time points at each temperature would be needed to extract meaningful physical parameters from this temperature dependence.

As distinguished from mean speed, **displacement** (μm/s) looks at the whole trajectory rather than each frame, and is the norm of the total XY path, D= $\sqrt{(\Delta x)^2 + (\Delta y)^2}$. For a straight track, displacement will equal mean speed $< v >$ multiplied by total time T of the track lifetime; for a circular track, displacement will be close to 0 regardless of mean speed. Dividing the displacement by $< v > T$ gives a dimensionless number that can be used to classify tracks. **Figure 7C** shows the average D/$< v > T$ vs temperature, and **Fig. 7 D** shows a histogram of displacements for selected measured tracks at multiple temperatures; values of D/$< v > T$ ≥0.55 indicated long runs.

Sinuosity is a measure of movement inefficiency defined as end-to-end displacement over total path length in µm. For a straight path, sinuosity will equal 1. For a serpentine or circular movement pattern, sinuosity will be >>1. Values of >20 were only seen at lower temperatures (**Fig. 7 E**). The cell-by-cell classifications in Table 1 agreed with this analysis, as circular tracks were not found in the elevated temperatures.

Acceleration ($\mu m/s^2$) is measured as inter-frame differences in velocity:

$$\overline{a} = \frac{1}{N}\sum_{i=i}^{N}\frac{\|\vec{v}_i-\vec{v}_{i-1}\|}{\Delta t} \quad (6),$$

and could be used along with mean speed to classify tracks. Long, smooth runs showed low values of acceleration, while tracks with multiple tumble events showed high values. Similarly, the **step angle** measures how much a particle turns at each time point. It gives the angle that a particle deviated from a straight path per inter-frame interval (in radians). Passively drifting particles should not vary much in their direction from frame to frame, while highly motile particles that swerve and turn regularly will show large changes in step angle. **Figure 7F** shows a correlation matrix of the measured parameters, showing that D/$< v > T$ showed a negative correlation with nearly all measured values.

Autocorrelations of speed, velocity, and turn angle at 1 and 2 seconds did not vary significantly among datasets (not shown; available in Supplementary Datasheets 2-7).

3.4 Surface clustering

At higher temperatures (60 ºC and above), cells were seen to be swimming above large patches of surface-adherent bacteria. The Z projections could not determine how far the highly motile cells were from the patches, or whether they were interacting. Thus, it was necessary to use full Z plane reconstructions to identify the relative position of motile cells vs. collections of non-motile cells at the chamber bottom. It was seen that the highly motile cells were moving at focal planes tens to hundreds of microns away from the chamber bottom (**Fig. 8 A, B, Supplementary Video 11)**. While some active motility was seen near the clustered cells at the surface, it was significantly slower as expected near a surface (Li et al., 2008;Li et al., 2011). Similar groups of cells were not seen with the killed sample (**Fig. 8 C**).

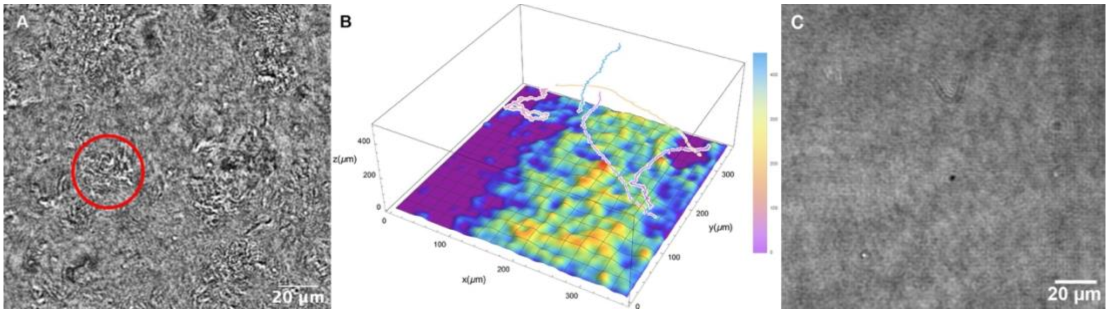

Figure 8. Collections of non-motile cells on the chamber surface at 66 ºC. (A) Still image; the circle indicates a cluster of cells. (B) Schematic of surface clustered cells with relative positions of selected motile tracks. (C) Corresponding image of the slide surface with the killed cell dataset at 66 ºC.

4 Discussion

The novel immersion system reported in this paper allows for recordings of bacterial motility up to nearly the boiling point of water. The custom software package that we report for the first time here aids in tracking of motile organisms as well as identification of non-motile tracks resulting from drift. Distinguishing drift from motility was straightforward by visual inspection, as active motility could occur perpendicular to the thermal drift. However, the automated algorithm did generate a large number of false positive tracks, so manual validation was essential to accurately identify motile organisms. The MHI images were used to help identify tracks that corresponded to organisms. Although human intervention is needed, this method is significantly easier than manual tracking. As HELM was designed for use on spacecraft, HELM can process a sample in several minutes on an ordinary laptop computer, and manual confirmation of motile tracks may be performed in less than an hour. It is important to note that the current implementation of the software assumes (and checks for) a constant frame rate, so it is necessary to ensure that the acquisition camera and software do not drop frames. Future versions of the software will enable input of a timestamps file to accommodate varying frame rates. An approach to extracting tracks directly from the MHI traces is also in development.

For this work, tracking was only performed on 2D projections of the 3D tracks. The errors introduced in velocities and turn angles by this approximation have been reported (Taute et al., 2015). Given that the axial resolution of the instrument is >2 μm, we decided that in this analysis, the additional computational and time cost of 3D tracking does not contribute significantly to the analysis of velocities, as we have shown in a previous analysis (Acres and Nadeau, 2021). In 2D, helices appear as spirals, with all of the parameters of the helix readily extractable from the 3D data (Gurarie et al., 2011). For organisms or instruments that show higher contrast, HELM could also be used on individual Z planes. However, with our current implementation, the signal to noise of *B. subtilis* is too low for tracking on a single plane, so projections over multiple planes were used. Since most literature data is based upon 2D tracks, this also allows for easier comparison of our measured speeds with those found in other studies. The speeds we observed, 15-25 μm/s, are consistent with the recent reports (Turner et al., 2016).

However, large variations from study to study have made general conclusions about parameters as simple as mean velocity for a given strain largely impossible. A new database, named BOSO-Micro (Rodrigues et al., 2021), is aiming to increase standardization of motility experiments and parameters. Such databases will be important for summarizing the large amounts of data being generated in the rapidly emerging field of bacterial tracking.

Using this system and approach, we found that *B. subtilis* was capable of active motility up to 66ºC under conditions of constant heating over a time course of 4 hours. Cell size and shape did not significantly change with temperature. The changes in speed with temperature were consistent with previous studies up to 50 ºC (Schneider and Doetsch, 1977), with data unavailable past that point. We observed active motility to 66 ºC, but with a minority of cells being motile at temperatures above ~45 ºC. The majority of cells were found clustered on the lower surface of the chamber at high temperatures. This is consistent with cell population heterogeneity in this species (Lopez et al., 2009) (Kearns and Losick, 2005) (Syvertsson et al., 2021a). In addition, some of the cells in this recording showed a change in the observed motility type, most commonly a change from run-and-tumble to long runs. These parameters were indicated by turn angles, total displacement, and sinuosity in our analysis. Tracks with high sinuosity, indicating circling, were seen only at the lower temperatures. Long runs could be readily identified from total displacement divided by average velocity and time length of the track. The observed effect may result from the highly nonlinear viscosity of water at high temperatures, but additional experiments are necessary to attempt to deconvolve viscosity and temperature.

After 66°C, movement in the field was due to thermal drift alone. The thermocouples used to confirm the temperature of the chamber showed a slight difference between the top and bottom glass of the chamber, which could have led to increased thermal currents, most notably at temperatures past the limit for autonomous motion. This drift was clearly distinguishable from active motility on the MHI traces, but attention to correct classification of tracks as motile or non-motile was essential during analysis. The algorithm performed well with the killed samples, identifying nearly all of the tracks as non-motile despite drift, although it did yield a small number of false positives at the highest temperature (84 ºC). The random forest classifier used to classify tracks as motile or non-motile relies upon numerous parameters, no single one of which is sufficient to classify a track as motile or non-motile. Further analysis will correlate physical parameters with motility; this may require analysis beyond the use of means and standard deviations across an entire track, but close attention to instantaneous parameters. This analysis will also aid in classifying motile tracks with regard to run length and tumble frequency. Custom training of the classification software may be necessary for datasets with substantially different flow profiles.

The MHI traces are a unique feature of HELM, which was designed with spaceflight missions in mind, where the detection of possible signs of life with the least possible processing power is required. The MHI allows visualization of tracks in low signal-to-noise recordings where objects cannot easily be identified by tracking algorithms. These traces may be used as a guide for selection of complete motile tracks identified by HELM. However, compared to other software packages such TrackMate, HELM's particle identification and tracking is less interactive. When the algorithms do not perform well, the MHI may be used as a guide to finding tracks manually or using other particle detection algorithms in other packages. When HELM's detection and tracking works well, tracks are exported in .json files which may be imported into other packages for stitching or further analysis.

Reconstruction at individual Z planes at higher temperatures showed rapidly swimming cells tens to hundreds of µm above the surface, with large numbers of cells on the surface, some of which exhibited active motility. The presence of active motility in mesophilic organisms at temperatures beyond those at which they can grow is somewhat of a surprising result. Direct visualization of the motion of individual cells in this work makes this result unambiguous. The use of killed control cells eliminated any possibility that the motion was due to complex thermal currents, and the disappearance of any signs of active motility above 66 ºC further indicates that the "live" cells became inactive at this point. When reduced viscosity at these temperatures was considered, there was a temperature-dependent reduction in flagellar force. This is likely due to protein denaturation, and longer incubation times at these elevated temperatures may eventually lead to complete loss of motility. More detailed experiments with controlled incubation times at specific temperatures may provide useful models of thermal stability of motility-related proteins (Daniel and Danson, 2010). This paper represents the first step towards evaluating the upper limits of temperature on mesophile motility.

The authors hope that this simple setup will encourage others to reproduce these experiments and examine other strains of bacteria and archaea. In contrast to bacteria, especially test strains such as *E. coli* and *B. subtilis*, hyperthemophilic archaea have not been frequently imaged. The setup we report here should facilitate studies of thermophilic organisms, including those such as *Pyrococcus furiosus* which require temperatures near the boiling point of water for optimal motility (Herzog and Wirth, 2012).

The detailed parts list, combined with the open-source software, should be sufficient to enable duplication of the system by anyone who wishes to perform these experiments. The only custom parts are a 3D printed stage and objective lens holder (plastic) and a custom machined stage (aluminum) to allow for easy changing of sample chambers without requiring stage realignment. CAD drawings of these can be provided on request, and users are encouraged to tailor designs to their own specific applications. It is important to ensure that these elements are made from materials that can withstand high temperatures; any materials chosen should ideally be tested beforehand by submerging them into hot water at the desired temperatures before use on the microscope.

Conflict of Interest

The authors declare that the research was conducted in the absence of any commercial or financial relationships that could be construed as a potential conflict of interest.

Author Contributions

MD and NJ: construction and calibration of thermal control apparatus; growth and maintenance of bacteria; data collection; data analysis; data archiving; writing. MW and JL: Development of HELM tracking software; troubleshooting and debugging of software and addition of new features upon request. CL: original concept design; acquisition of funding. JN: acquisition of funding; supervision and planning of experiments; data analysis; writing. All authors: editing and approval of final draft.

Funding

The authors acknowledge the support of the National Science Foundation Grant Number 1828793. Portions of this work were supported under a contract from, or performed at, the Jet Propulsion Laboratory, California Institute of Technology, under a contract with the National Aeronautics and Space Administration.

5 References

Acres, J., and Nadeau, J. (2021). 2D vs 3D Tracking in Bacterial Motility Analysis. *AIMS Biophysics* 8**,** 385-399.

Armstrong, D.J., Nieminen, T.A., Favre-Bulle, I., Stilgoe, A.B., Lenton, I.C.D., Schembri, M.A., and Rubinsztein-Dunlop, H. (2020). Optical Force Measurements Illuminate Dynamics of Escherichia coli in Viscous Media. *Frontiers in Physics* 8. doi: 10.3389/fphy.2020.575732.

Bedrossian, M., Wallace, J.K., Serabyn, E., Lindensmith, C., and Nadeau, J. (2020). Enhancing final image contrast in off-axis digital holography using residual fringes. *Opt Express* 28**,** 16764-16771. doi: 10.1364/OE.394231.

Breiman, L. (2001). Random Forests. *Machine Learning* 45**,** 5-32. doi: 10.1023/A:1010933404324.

Cairns, L.S., Marlow, V.L., Kiley, T.B., Birchall, C., Ostrowski, A., Aldridge, P.D., and Stanley-Wall, N.R. (2014). FlgN Is Required for Flagellum-Based Motility by Bacillus subtilis. *Journal of Bacteriology* 196**,** 2216-2226. doi: 10.1128/jb.01599-14.

Charles-Orszag, A., Lord, S.J., and Mullins, R.D. (2021). High-Temperature Live-Cell Imaging of Cytokinesis, Cell Motility, and Cell-Cell Interactions in the Thermoacidophilic Crenarchaeon Sulfolobus acidocaldarius. *Front Microbiol* 12**,** 707124. doi: 10.3389/fmicb.2021.707124.

Cohoe, D., Hanczarek, I., Wallace, J.K., and Nadeau, J. (2019). Multiwavelength imaging and unwrapping of protozoa in amplitude and phase using custom Fiji plug-ins. *Frontiers in Physics* in press.

Daniel, R.M., and Danson, M.J. (2010). A new understanding of how temperature affects the catalytic activity of enzymes. *Trends Biochem Sci.* 35**,** 584-591.

Demir, M., and Salman, H. (2012). Bacterial Thermotaxis by Speed Modulation. *Biophysical Journal* 103**,** 1683-1690. doi: 10.1016/j.bpj.2012.09.005.

Giacche, D., Ishikawa, T., and Yamaguchi, T. (2010). Hydrodynamic entrapment of bacteria swimming near a solid surface. *Phys Rev E Stat Nonlin Soft Matter Phys* 82**,** 056309. doi: 10.1103/PhysRevE.82.056309.

Gluch, M.F., Typke, D., and Baumeister, W. (1995). Motility and thermotactic responses of Thermotoga maritima. *J Bacteriol* 177**,** 5473-5479. doi: 10.1128/jb.177.19.5473-5479.1995.

Gurarie, E., Grunbaum, D., and Nishizaki, M.T. (2011). Estimating 3D Movements from 2D Observations Using a Continuous Model of Helical Swimming. *Bulletin of Mathematical Biology* 73**,** 1358-1377. doi: 10.1007/s11538-010-9575-7.

Hecker, M., Schumann, W., and Volker, U. (1996). Heat-shock and general stress response in Bacillus subtilis. *Molecular Microbiology* 19**,** 417-428. doi: 10.1046/j.1365-2958.1996.396932.x.

Herzog, B., and Wirth, R. (2012). Swimming Behavior of Selected Species of Archaea. *Applied and Environmental Microbiology* 78**,** 1670-1674. doi: 10.1128/aem.06723-11.

Humphries, S. (2013). A physical explanation of the temperature dependence of physiological processes mediated by cilia and flagella. *Proceedings of the*

National Academy of Sciences of the United States of America 110**,** 14693-14698. doi: 10.1073/pnas.1300891110.

Jaqaman, K., Loerke, D., Mettlen, M., Kuwata, H., Grinstein, S., Schmid, S.L., and Danuser, G. (2008). Robust single-particle tracking in live-cell time-lapse sequences. *Nat Methods* 5**,** 695-702. doi: 10.1038/nmeth.1237.

Kearns, D.B., and Losick, R. (2005). Cell population heterogeneity during growth of Bacillus subtilis. *Genes & Development* 19**,** 3083-3094. doi: 10.1101/gad.1373905.

Li, G., Bensson, J., Nisimova, L., Munger, D., Mahautmr, P., Tang, J.X., Maxey, M.R., and Brun, Y.V. (2011). Accumulation of swimming bacteria near a solid surface. *Phys Rev E Stat Nonlin Soft Matter Phys* 84**,** 041932. doi: 10.1103/PhysRevE.84.041932.

Li, G., Tam, L.K., and Tang, J.X. (2008). Amplified effect of Brownian motion in bacterial near-surface swimming. *Proc Natl Acad Sci U S A* 105**,** 18355-18359. doi: 10.1073/pnas.0807305105.

Lopez, D., Vlamakis, H., and Kolter, R. (2009). Generation of multiple cell types in Bacillus subtilis. *Fems Microbiology Reviews* 33**,** 152-163. doi: 10.1111/j.1574-6976.2008.00148.x.

Maeda, K., Imae, Y., Shioi, J.I., and Oosawa, F. (1976). EFFECT OF TEMPERATURE ON MOTILITY AND CHEMOTAXIS OF ESCHERICHIA-COLI. *Journal of Bacteriology* 127**,** 1039-1046. doi: 10.1128/jb.127.3.1039-1046.1976.

Magariyama, Y., and Kudo, S. (2002). A mathematical explanation of an increase in bacterial swimming speed with viscosity in linear-polymer solutions. *Biophysical Journal* 83**,** 733-739. doi: 10.1016/s0006-3495(02)75204-1.

Mann, C., Yu, L., Lo, C.M., and Kim, M. (2005). High-resolution quantitative phase-contrast microscopy by digital holography. *Opt Express* 13**,** 8693-8698. doi: 10.1364/opex.13.008693.

Moliere, N., Hossmann, J., Schafer, H., and Turgay, K. (2016). Roleo f Hsp100/Clp Protease Complexes in Controlling the Regulation of Motility in Bacillus subtilis. *Frontiers in Microbiology* 7. doi: 10.3389/fmicb.2016.00315.

Mukherjee, S., and Kearns, D.B. (2014). "The Structure and Regulation of Flagella in Bacillus subtilis," in *Annual Review of Genetics, Vol 48,* ed. B.L. Bassler.), 319-340.

Nannapaneni, P., Hertwig, F., Depke, M., Hecker, M., Mader, U., Volker, U., Steil, L., and Van Hijum, S. (2012). Defining the structure of the general stress regulon of Bacillus subtilis using targeted microarray analysis and random forest classification. *Microbiology-Sgm* 158**,** 696-707. doi: 10.1099/mic.0.055434-0.

Nishiyama, M., and Arai, Y. (2017). Tracking the Movement of a Single Prokaryotic Cell in Extreme Environmental Conditions. *Methods Mol Biol* 1593**,** 175-184. doi: 10.1007/978-1-4939-6927-2_13.

Peterson, M.E., Daniel, R.M., Danson, M.J., and Eisenthal, R. (2007). The dependence of enzyme activity on temperature: determination and validation of parameters. *Biochem J* 402**,** 331-337. doi: 10.1042/BJ20061143.

Pulschen, A.A., Mutavchiev, D.R., Culley, S., Sebastian, K.N., Roubinet, J., Roubinet, M., Risa, G.T., Van Wolferen, M., Roubinet, C., Schmidt, U., Dey, G., Albers, S.V., Henriques, R., and Baum, B. (2020). Live Imaging of a Hyperthermophilic Archaeon Reveals Distinct Roles for Two ESCRT-III Homologs in Ensuring a Robust and Symmetric Division. *Curr Biol* 30**,** 2852-2859 e2854. doi: 10.1016/j.cub.2020.05.021.

Riekeles, M., Schirmack, J., and Schulze-Makuch, D. (2021). Machine Learning Algorithms Applied to Identify Microbial Species by Their Motility. *Life-Basel* 11. doi: 10.3390/life11010044.

Rodrigues, M.F.V., Lisicki, M., and Lauga, E. (2021). The bank of swimming organisms at the micron scale (BOSO-Micro). *Plos One* 16. doi: 10.1371/journal.pone.0252291.

Schindelin, J., Arganda-Carreras, I., Frise, E., Kaynig, V., Longair, M., Pietzsch, T., Preibisch, S., Rueden, C., Saalfeld, S., Schmid, B., Tinevez, J.Y., White, D.J., Hartenstein, V., Eliceiri, K., Tomancak, P., and Cardona, A. (2012). Fiji: an open-source platform for biological-image analysis. *Nature Methods* 9**,** 676-682. doi: 10.1038/nmeth.2019.

Schneider, W.R., and Doetsch, R.N. (1977). TEMPERATURE EFFECTS ON BACTERIAL MOVEMENT. *Applied and Environmental Microbiology* 34**,** 695-700. doi: 10.1128/aem.34.6.695-700.1977.

Schumann, W. (2003). The Bacillus subtilis heat shock stimulon. *Cell Stress & Chaperones* 8**,** 207-217. doi: 10.1379/1466-1268(2003)008<0207:Tbshss>2.0.Co;2.

Syvertsson, S., Wang, B., Staal, J., Gao, Y., Kort, R., and Hamoen, L.W. (2021a). Different Resource Allocation in a Bacillus subtilis Population Displaying Bimodal Motility. *J Bacteriol* 203**,** e0003721. doi: 10.1128/JB.00037-21.

Taute, K.M., Gude, S., Tans, S.J., and Shimizu, T.S. (2015). High-throughput 3D tracking of bacteria on a standard phase contrast microscope. *Nature Communications* 6. doi: 10.1038/ncomms9776.

Turner, L., Ping, L., Neubauer, M., and Berg, H.C. (2016). Visualizing Flagella while Tracking Bacteria. *Biophys J* 111**,** 630-639. doi: 10.1016/j.bpj.2016.05.053.

Wagner, T., Lipinski, H.G., and Wiemann, M. (2014). Dark field nanoparticle tracking analysis for size characterization of plasmonic and non-plasmonic particles. *J Nanopart Res* 16**,** 2419. doi: 10.1007/s11051-014-2419-x.

Wallace, J.K., Rider, S., Serabyn, E., Kuhn, J., Liewer, K., Deming, J., Showalter, G., Lindensmith, C., and Nadeau, J. (2015). Robust, compact implementation of an off-axis digital holographic microscope. *Optics Express* 23**,** 17367-17378. doi: 10.1364/oe.23.017367.

Warth, A.D. (1978). Relationship between the heat resistance of spores and the optimum and maximum growth temperatures of Bacillus species. *J Bacteriol* 134**,** 699-705. doi: 10.1128/jb.134.3.699-705.1978.

Young, J.W., Locke, J.C.W., and Elowitz, M.B. (2013). Rate of environmental change determines stress response specificity. *Proceedings of the National Academy of Sciences of the United States of America* 110**,** 4140-4145. doi: 10.1073/pnas.1213060110.

Zottl, A., and Yeomans, J.M. (2019). Enhanced bacterial swimming speeds in macromolecular polymer solutions. *Nature Physics* 15**,** 554-+. doi: 10.1038/s41567-019-0454-3.

Appendix A: Supplemental Materials for Chapter 3

Supplementary Methods: Description of immersion setup with detailed instructions, including Supplementary Figures S9-S10 (photos of setup) and Figures S11-S13 (sample chambers). Figure S14: MHI output for killed cells at selected temperatures. Figure S15: Reproducibility of replicate datasets.

Supplementary Videos: 11 (captions given in Supplementary Material, pg 89-90). Can be found on the journal site.

Supplementary datasheet: listed as tables 1-7 and found at: https://www.frontiersin.org/articles/10.3389/fmicb.2022.836808/full#supplementary-material

Supplementary Methods

System Assembly and Use

The parts used in construction of this system are listed in **Supplementary Datasheet 1**. Complete and detailed microscope assembly can be found in U.S. Patent US20160131882A1 and in the following reference: Wallace, J.K., Rider, S., Serabyn, E., Kuhn, J., Liewer, K., Deming, J., Showalter, G., Lindensmith, C., and Nadeau, J. (2015). Robust, compact implementation of an off-axis digital holographic microscope. *Optics Express* 23**,** 17367-17378. doi: 10.1364/oe.23.017367. This section outlines the assembly and use of the microscope and heat bath system. Items in this section are referenced by the 'ref number' in **Supplementary Datasheet 1**.

After microscope assembly, the system must be prepared for submersion and exposure to increasing temperatures, so several precautions must be taken. Previous iterations of the experimental design led to water infiltrating the microscope components, non-viable fiber optic cables, and condensation on the surface of the optics and sample chambers.

First, a housing around the collimator and up to the microscope stage was necessary. It was found that water pressure would push the bags surrounding the microscope into the space between the microscope stage and collimator, blocking the light from the laser. This was solved by custom fitting the Newark Minibox metal enclosure (42) to the microscope. The box was assembled, and one side was removed to serve as the top, which sits just below the microscope stage. On one of the sides adjacent to the removed top, notches were cut so the box slid up around the arms holding the collimator to the base of the microscope. For this setup, the notches are shown in **Figure S9**. This allows the enclosure to slide parallel to the base of the microscope and sit just below the stage. It is important to check that the enclosure is long enough to: a) cover the gap between the collimator and microscope stage, and b) give the fiber optic cable enough room to loosely sit below the collimator and curve to exit out the top of the enclosure without bending or warping the cable.

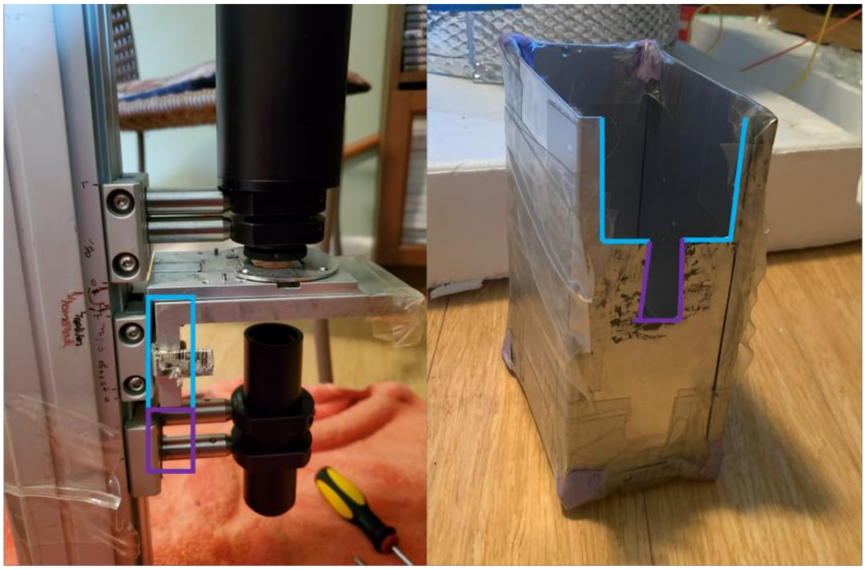

Figure S9. Microscope adjustments. Notches cut into metal enclosure to fit around base of the microscope stage and the collimator attachment. Metal enclosure should sit slightly below the stage when attached.

Once the notches have been cut in the enclosure, any sharp edges on the enclosure need to be covered to prevent tearing of the bags. Any substance which covers the sharp edges is fine, but it should be one that will not degrade with exposure to high temperatures. In this case, torn nitrile lab gloves were layered around the corners to act as a bumper and then held in place with heat-resistant carpet tape. This was done in layers to ensure any sharp edges were covered. The heat-resistant tape was then put along all sides of the enclosure, even the machined edges. The tape was then used to secure the enclosure to the base of the microscope. The enclosure should be adhered in a way that is stable enough to withstand the experiment, but also allow for easy removal in case of accidents or maintenance.

Once the enclosure is attached to the microscope, the system is ready for submersion. First, place the sample chamber on the stage and make sure it is fixed in place. Take some sample recordings to check the focus since it cannot be adjusted later without removing the microscope from the heat bath. The Ziploc bags (41) are recommended. They were able to withstand boiling without degradation and breaking. In initial iterations of the experiment, autoclave bags were used. These are less durable but do provide a more flexible barrier than the Ziploc bags. If using autoclave bags, the bags should definitely be double layered around the microscope, since degradation after prolonged exposure was an issue. Fill the majority of the pot (40) with water before placing the microscope in. Submerge the microscope and bags until the bottom of the base is at the bottom of the pot. Using an F-clamp, clamp the base of the microscope to the outside of the pot. After the clamp is tightened, check to be sure the stage of the microscope is at a level that is still within the pot. Attach the sous vide (39) to the opposite side of the pot and fill the pot with water until the level is at least 1” above the microscope stage. Insert dowel-like objects (kitchen spatulas/spoons work just fine) into the space between the metal enclosure and the stage, and stick out of the top of the bags and pot. This is to prevent condensation from forming on the surface of the sample chamber or any of the optics.

The pot should be placed on an insulating surface, since heat loss from the pot can reach the same order of magnitude as the rate at which the sous vide heats the water. This was noted primarily at temperatures >~66C. In this setup, a Styrofoam block several inches thick was used. To insulate the sides, wrap the exterior of the pot in insulating material (metallized bubble wrap bags from Imperfect Foods worked well when cut to form a single long strip). Wrap the material tightly and adhere with heat-resistant adhesive. The pot will be very hot as the experiment progresses, so having a tape that will withstand that is important. Carpet tape is a good option. Lastly, cut insulating material to form a cover for the bath. The imperfect food bag can be cut along the seam until it resembles a tent with flaps on one side. Place the "closed" end of the tent over the top of the pot at the side with the sous vide, so the flaps wrap around the column of the microscope. Make sure not to put the insulating material over the camera, as condensation will occur. This is to keep heat in from the top of the pot, critical for temps >~78C. The stages of wrapping the pot and submerging the microscope are shown in **Figure S10**.

Figure S10. Insulation for heated bath. Progression of insulating the pot and submerging the microscope, from left to right.

Sample chambers

The sample chambers used in the experiment were custom designed, as referenced in the methods section. However, this system was also tested with sample chambers that are simpler and can be made quickly in the laboratory. This section outlines the construction of simple, effective sample chambers that have been tested and are suitable for use at the range of temperatures described. They were made to contain both a sample and reference channel that are filled separately. They consist of optically clear glass tops and bottoms, with a gas-permeable layer giving depth to the chamber, as shown in **Figure S11**.

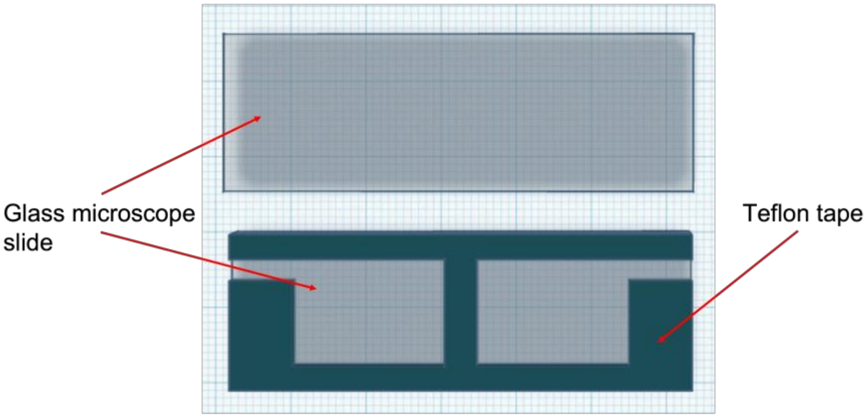

Figure S11. Sample chamber model. Model of the component pieces of a simple, custom sample chamber for DHM. The glass slides form the top and bottom of the chamber and the teflon tape is cut to form the sample and reference wells. The chamber depth is 0.5mm.The chambers are made from two 25mm x 75mm x 1mm glass microscope slides (Fisherbrand or other) and a piece of 0.5mm thick Teflon tape (CS Hyde, Item #: 15-20HB-DS-1-5, .020" Skived PTFE w/ High Bond) cut to the same dimensions as the microscope slides.

The Teflon is then cut in the shape shown (**Figures S11, S12**), with the central barrier ~4mm wide. For the instrument used in this experiment and described in Supplementary Datasheet 1, the separation of the objective lenses is 6.0 mm, so this middle barrier should not exceed this distance. A channel was also cut to the edges of the Teflon for the wells to be filled once the chamber was completely assembled.

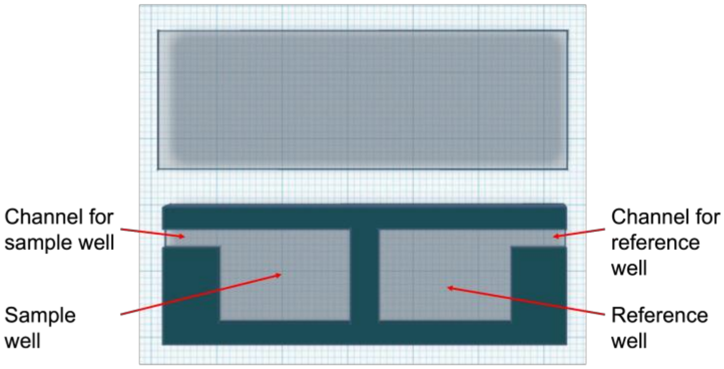

Figure S12. Chamber model details. Modeled setup of sample chamber with separate sample and reference wells. Designed with channels for filling after chamber construction to prevent bubbles. Middle barrier separating the wells should be thinner than the separation of the objective lenses of the microscope. For the microscope used here, that is less than 6.0mm.

Adhesive was placed along the bottom side of the Teflon to adhere it to one of the microscope slides. Once the adhesive is set, apply adhesive to the top side of the Teflon and adhere the other microscope slide. Dow Corning high vacuum grease can also be used, but is less stable because it does not solidify. Allow to sit while the adhesive cures. The completed setup is shown (**Figure S13**).

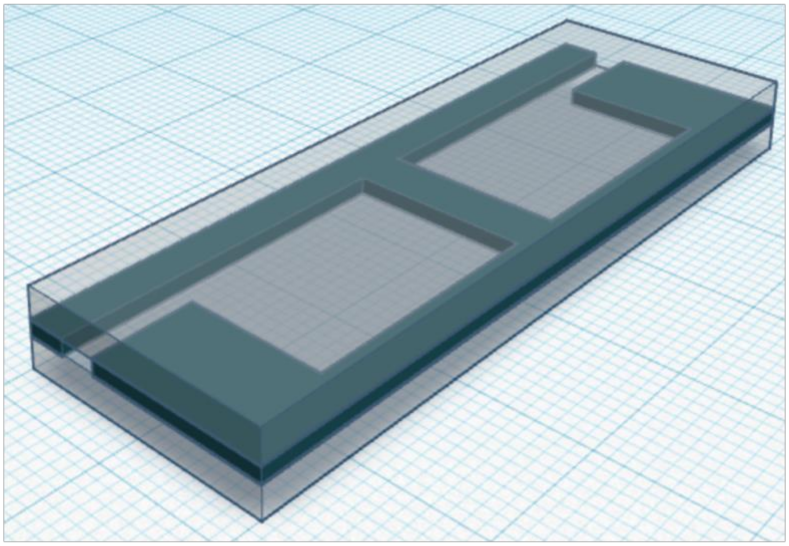

Figure S13. Assembled chamber model. Model of the completed chamber described in this section. Gaps from the channel should be filled with sealant or vacuum grease to prevent leaking and bubbles.

When ready for use, inject the specimen into the sample well using a needle. Once the well is filled, seal the channel. Silicone sealant or high vacuum grease recommended. Repeat these steps with the reference well and adhere the chamber to the stage before proceeding.

Supplementary Data

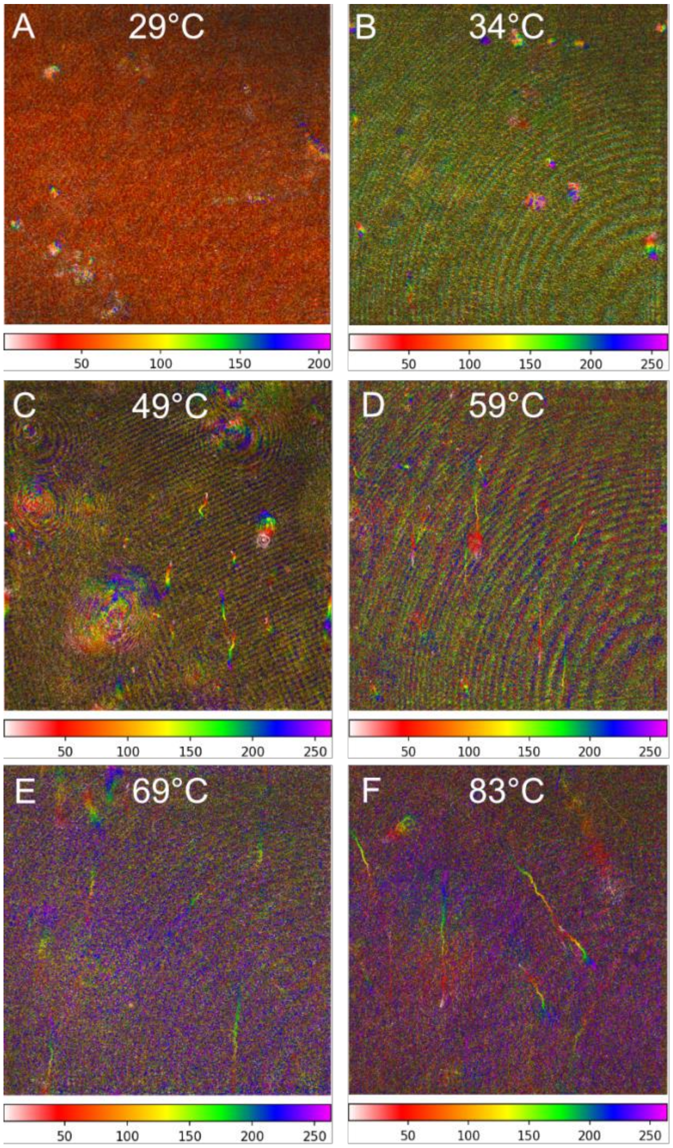

Figure S14. MHI tracks from killed *B. subtilis* at different temperatures. The field of view is 365 x 365 µm and the color scales indicate time in frames (15 frames/s).

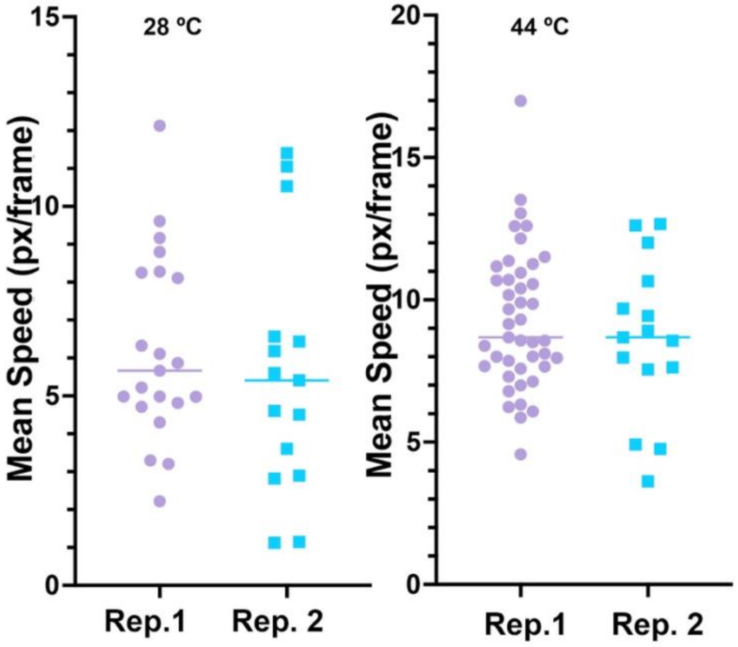

Figure S15. Consistency between replicate experiments. Examples of mean speeds from 2 replicates done on independent days, showing consistency of values.

Video captions

Supplementary Video 1. Example of automated tracker using a 34 ºC data set. Tracks in cyan are identified by the software as non-motile, and those in magenta as motile. Tracks were handpicked and re-classified as necessary, using the MHI as a guide in order to match identified tracks to organisms.

Supplementary Video 2. Portion of a single plane reconstruction at 28 ºC. 250 frames at 15 frames/s.

Supplementary Video 3. Portion of a single plane reconstruction at 34 ºC. 250 frames at 15 frames/s.

Supplementary Video 4. Portion of a single plane reconstruction at 44 ºC. 250 frames at 15 frames/s.

Supplementary Video 5. Portion of a reconstruction 180 µm above the plane of the slide at 61 ºC. 250 frames at 15 frames/s.

Supplementary Video 6. Maximum z-projection at 66 ºC. 250 frames at 15 frames/s.

Supplementary Video 7. Portion of a single plane reconstruction at 84 ºC. 250 frames at 15 frames/s.

Supplementary Video 8. Killed cells, single plane reconstruction at 28 ºC. 260 frames at 15 frames/s.

Supplementary Video 9. Killed cells, single plane reconstruction at 84 ºC. 260 frames at 15 frames/s.

Supplementary Video 10. Results of HELM tracker and classifier with killed cells at 84 ºC. 260 frames at 15 frames/s. Tracks in cyan are identified by the software as non-motile, and those in magenta as motile.

Supplementary Video 11. Portion of a reconstruction at the plane of the slide at 61 ºC. 250 frames at 15 frames/s.

Data Availability Statement

The raw holograms for the datasets used here are deposited in a public depository at Data Dryad, accession https://doi.org/10.5061/dryad.ns1rn8pv6. Other data are available from the authors upon request. The software packages used are all open source and are available at the following sites:

DHMx: https://github.com/dhm-org/dhm_suite

HELM: https://github.com/JPLMLIA/OWLS-Autonomy

Reconstruction Fiji plug-ins: https://github.com/sudgy/

Chapter 4: Substrate Considerations for Digital Holographic Microscopy Cell Tracking Applications

Note: This work is the article “Substrate considerations for digital holographic microscopy cell tracking applications” that is written with the intent of publication. It is the work of Megan Dubay, Eugene Serabyn, J. Kent Wallace, Manuel Bedrossian, Chris Lindensmith, and Jay Nadeau. The target journal is *Biomedical Optics Express.* At time of publication of this thesis, it will be submitted for publication and under review. This chapter is formatted in the way required by the target journal.

Citation: Dubay MM, Serabyn G, Lindensmith, CA, Nadeau JL. “Substrate considerations for digital holographic microscopy cell tracking applications.” In progress for submission to *Biomedical Optics Express,* 2022.

It focuses on material considerations for imaging using digital holographic microscopy. Special material considerations may be needed for a specific environment to be tested, such as the prospect of sending organisms to the International Space Station for study of how microbes change under the influence of microgravity. Due to the nature of the ISS as a closed ecosystem, limitations are imposed for astronaut safety. Materials that are commonly used for microscopy can be hazardous in this new environment, and alternative solutions were developed. As a precursor for the development of sample chambers certified for flight on the ISS, a detailed look at several optically clear substrates was required. This chapter examines the characteristics of several imaging materials—including glass, vinyl, and polymers. Work described within was completed, in part, at Jet Propulsion Laboratory, California Institute of Technology and under contract with the National Aeronautics and Space Administration. This investigation was funded, in part, through an ISS National Laboratory Research Announcement focused on technology development put forth by the Center for the Advancement of Science in Space.

Author Contributions: MD: data acquisition and analysis, construction of sample chambers, growth and maintenance of bacteria, writing. ES: theory. CL: theory, acquisition of funding. JN: acquisition of funding; supervision and planning of experiments; data analysis; writing. All authors: editing and approval of final draft.

Substrate Considerations for Digital Holographic Microscopy Cell Tracking Applications

Megan Dubay,[1] Eugene Serabyn[2], Chris Lindensmith,[2] and Jay L. Nadeau[1*]
[1]Portland State University, Department of Physics, 1719 SW 10th Ave., Portland, OR 97201, USA; *[2]Jet Propulsion Laboratory, California Institute of Technology, 4800 Oak Grove Dr., Pasadena, CA 91109, USA*

Abstract

Digital holographic microscopy (DHM) is an emerging light microscopic technique that enables both phase and amplitude imaging, useful for label-free visualization of biological cells. While instrumentation for DHM has been well developed, little attention has been paid to the influence of substrate composition, thickness, and quality on the ability to detect small cells and to quantify phase for quantitative phase imaging (QPI). In this study, we evaluate different substrates used to create sample chambers for DHM of bacterial cells in suspension. Phase noise, fringe visibility, and signal-to-noise ratio of individual bacterial cells inside the chambers are used to evaluate image quality. We find that the use of polymers such as polydimethylsiloxane (PDMS) and polycarbonate as substrate material introduces complex phase noise to measurements, and these materials are deemed incompatible with QPI. Vinyl shows an acceptable profile though significantly lower signal to noise than glass. High quality solid etalons show a superior wavefront quality compared with microscope slides, though this does not translate into higher signal to noise because of the ability to remove aberrations using a reference hologram. These results have implications for design of reusable and disposable substrates for imaging and tracking of biological samples.

1 Introduction

Amplitude (or intensity) imaging (brightfield microscopy) is the oldest and still one of the most useful methods in cell and molecular biology. However, many biological cells do not absorb or scatter light appreciably. Methods of increasing contrast in biological light microscopy either add absorptive features to specific structures (using dyes and stains) or take advantage of the phase shift produced by the cell structures' different refractive indices in order to distinguish specimen from background [1, 2]. Phase contrast microscopy was developed in the 1930s, and remains an important technique in light microscopy [3, 4]. However, typical Zernike phase contrast does not provide quantitative information about the phase shift produced by the object. Methods of quantifying this shift are referred to as quantitative phase imaging (QPI) or quantitative phase microscopy, and are implemented using a variety of interferometric techniques [5-7].

One commonly used technique for both brightfield and QPI in biology is off-axis digital holographic microscopy (DHM), which records the interference of a reference beam and a beam passing through the specimen. This pattern, or hologram, is then reconstructed into amplitude and phase images at selected planes through the depth of the sample [8]. Intensity images (amplitude squared) are comparable to those made with conventional imaging microscopy, but phase images, which display the index of refraction variations in the specimen, have no conventional analog. Hilbert phase microscopy (HPM) is similar, but is designed for optically thin specimen, as it records the interferogram in the image plane [9]. Other approaches include Digitally Recorded Interference Microscopy with Automatic Phase Shifting (DRIMAPS) and Oblique Plane Microscopy (OPM) [10-13], as well as a variety of common-path techniques; these are well reviewed in [14].

DHM phase imaging has been used with cultured cells to measure changes in dry mass, which can indicate pathophysiological processes such as apoptosis, ion channel opening and closing, and response to osmotic shock [15-20]. Differences in phase ($\Delta\phi$) at a point *(x,y)* indicate areas that are different from water, as they are proportional to the difference in index of refraction between the medium (n_m) and the cell (n_c) times the thickness (h) of the specimen [21]:

$$\Delta\phi(x,y) = \frac{2\pi}{\lambda} h(x,y)[n_c(x,y) - n_m \quad (1)$$

The fundamental limit of sensitivity of an interferometric measurement is given by

$$\sigma_\phi = \sqrt{\langle(\Delta\phi)^2\rangle} = \frac{\sqrt[\sqrt{2}]{N + B + M\sigma_{rn}^2}}{VN} = \frac{1}{SNR} \quad (2)$$

where *N* is the number of photons per sample, *B* is the background, *M* is the number of reads, σ_{rn} is the read noise variance, *V* is the fringe visibility, and *SNR* is the signal to noise ratio. If the background and number of reads are neglected, this may be approximated as

$$\sigma_\phi \approx \frac{\sqrt{2}}{V\sqrt{N}} \quad (3)$$

The limits to phase imaging are thus the number of photons delivered to the sample and the fringe visibility. If samples are rapidly moving and so integration is not possible, the number of photons is limited by the detector. Because $n_c(x, y) - n_m$ for bacterial cells is ~0.03, rapid imaging of motile cells is at the limit of detection in phase for typical laser and camera systems.

The fringe visibility may also play a significant role in the ability to see and track cells. A significant source of noise in the phase reconstruction of holographic images arises from the material used to contain the sample being investigated, which has not yet been well documented. Microfluidic channels made of polymers such as polydimethylsiloxane (PDMS) are often used to contain cells for light microscopy, due to ease of fabrication and relatively low effect on light intensity imaging [22, 23]. PDMS channels have also been used for DHM, though no QPI was performed [24]. Other types of polymers are also available and are often marketed for high-resolution imaging, with testing performed using fluorescence techniques, including super-resolution techniques.

There are many reasons to choose polymers over glass for imaging. One is the ease of casting into complex micropatterns and of bonding to other materials. Another is safety for use under extreme conditions. For example, on the International Space Station (ISS), glass shards pose a serious risk to the crew under microgravity conditions, where the fragments may float and can cause injury. The use of unbreakable sample chamber materials greatly facilitates sample chamber design (requiring fewer levels of containment) and simplifies crew handling procedures. Another consideration is gas permeability; gas-permeable chambers allow aerobic organisms to be stored for long-term shipment or imaging.

The ultimate question in microscopy is whether the target samples can be successfully imaged. Noise is only a problem if it cannot be subtracted from the signal without losing or degrading the signal. Raw DHM images are usually too noisy to be of use, and images are only shown after significant processing. Sources of noise in DHM apart from the substrate include the imaging optics, vibrations, laser speckle, temporal phase noise that results from uncorrelated noise between the two fields of the interferometer, as well as noise introduced by the imaging device. Both pre- and post-processing filtering methods are used to reduce noise. The use of a reference hologram removes aberrations due to the optics [25]. The setup may be optimized by reducing the recording distance and using a camera with a smaller pixel size [26]. Other methods to reduce noise include phase error compensation, spatial light modulation (SLM), and multiple frequency overlapping [27-30], which improve the reconstructed phase image of holograms. Noise reduction is also accomplished by filtering certain frequencies, both in the spatial and Fourier planes, with Butterworth filters and masks, respectively [31-33]. In addition, efficient encoding methods and correlation based de-noising algorithms have been developed to significantly reduce speckle noise [34, 35]. During biological studies, the power of the light source must sometimes be monitored as to not harm the organisms being observed. This has prompted investigation into the reduction of errors introduced by shot noise that becomes significant at low illumination [36, 37]. Noise reduction techniques for phase imaging have been recently reviewed [38]. All of these noise reduction techniques may reduce signal, and when the signal is at the limit of detection, may eliminate it entirely.

In this work, we quantify the phase noise in off-axis digital holographic microscopy due to various substrate types and configurations ranging from glass and polymer microscope slides to molded PDMS substrates. Chamber noise is analyzed using the Power Spectral Density function (PSD), a radial average of the Fourier transform of the reconstructed phase image without aberration correction. The fringe visibility is also measured for each substrate. The effect of substrate phase noise on cell imaging is evaluated by calculating the signal to noise ratio (SNR) of samples of unpigmented bacteria of different sizes (*Bacillus subtilis* and *Vibrio alginolyticus*) in reconstructions with noise subtraction.

2 Methods and Materials

2.1 Digital Holographic Microscopy and Data Acquisition

A custom off-axis DHM instrument was used for this work, described previously[39] (**Fig. 1).** The effective magnification is 19.7 with a diffraction limited lateral resolution of 0.8 μm at 405 nm illumination. The illumination wavelength supplied by a single-mode, fiber-coupled diode laser that is collimated before the sample (Thorlabs MCLS-1, wavelength choices 405 nm or 520 nm). The camera was an Allied Vision Prosilica GT 2450 camera (3.45 μm/pixel) powered by Power over Ethernet (PoE). Acquisition speed was 15 frames per second with all frames measuring 2048x2048 pixels. Acquisition software was the open source DHMx package (https://github.com/dhm-org/dhm_suite) running on Ubuntu 18.04.5 LTS, on a Dell laptop with 31.1 GB of RAM and 2.0 GHz x12.

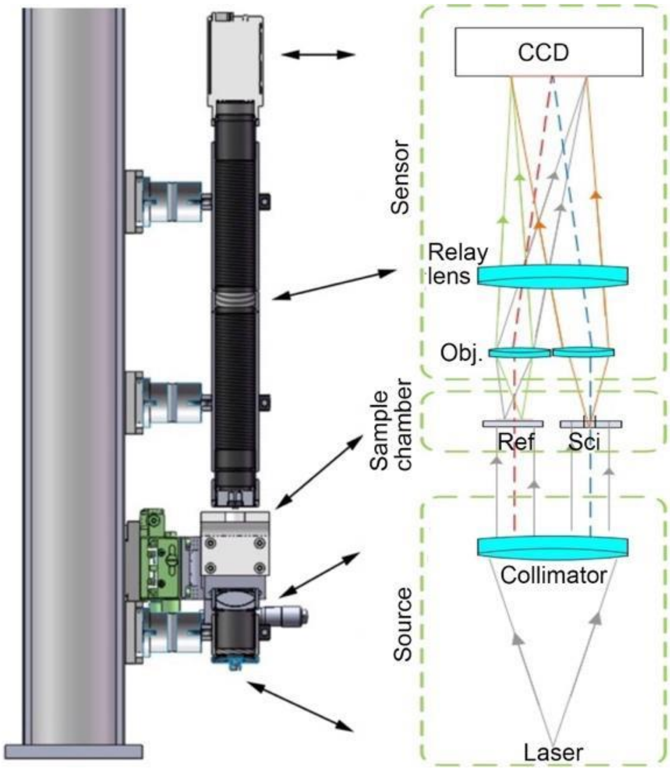

Fig. 1. Off-axis common-path DHM used in this study. Shown are a solid model and a schematic illustrating the source (single-mode laser illumination and collimating lens), the sample chamber (separated into reference [Ref.] and science [Sci.] chambers), and the sensor (consisting of paired aspheric objective lenses, a relay lens, and a CCD).

2.2 Data Processing

Holograms were reconstructed in amplitude and phase using the "DHM Utilities" plug-ins in FIJI which we have developed and published previously [40, 41]. Reconstruction uses the angular spectrum method, which has been shown to have advantages over other methods for quantitative phase microscopy[42]. Aberration correction by use of a reference hologram was not used for measurements of phase noise, but was used for phase reconstructions containing cells[25]. The reference hologram chosen was the median of the entire time series of holograms in each recording. Amplitude reconstruction was performed without a reference hologram but with tilt correction as described [43].

Phase noise was evaluated by reconstruction without reference hologram correction at and z= +40 µm (to avoid the singularity that occurs at z=0). The power spectral density P of the resulting images was calculated as the squared normalized Fourier transform [44, 45]; for the full two-dimensional image,

$$P\left(\omega_x, \omega_y\right) = \frac{|\mathfrak{F}\left(\phi(x,y)\right)|^2}{f_s N_x N_y} \quad (4)$$

where $P\left(\omega_x, \omega_y\right)$ is a function of spatial frequency in the x and y directions, $\mathfrak{F}$ is the Fourier transform operator, $\phi(x,y)$ is the phase image, f_s is the spatial sampling frequency at the focal plane, and N_x and N_y are the number of pixels in the x and y directions, respectively. Radial averaging condenses the PSD into a one-dimensional function. The radially averaged PSD function is defined as

$$\bar{P}_r(\omega_r) = \frac{\int_0^{2\pi} P(\omega_r, \omega_\theta) d\theta}{\int_0^{2\pi} \omega_r d\theta} \quad (5)$$

where $P(\omega_r, \omega_\theta)$ is the $P\left(\omega_x, \omega_y\right)$ from Equation 2 expressed in polar coordinates. Integrating $\bar{P}_r(\omega_r)$ across all spatial frequencies results in the variance, or net power, of the image. The net power is [44, 45]

$$\sigma^2 = 2\int_0^{\omega_m} \bar{P}_r(\omega_r) d\omega \quad (6)$$

where ω_m is the maximum spatial frequency that can be imaged by the camera, dictated by the Nyquist-Shannon sampling theorem.

The Fourier transform and radial averaging were performed in Fiji using the FFT and Radial Profile functions. The resulting spectra were plotted as a function of wavenumber using Prism 9 (GraphPad software, now part of Dotmatics, San Diego, CA). Fringe visibility V was calculated as

$$V = \frac{I_{max} - I_{min}}{I_{max} + I_{min}} \quad (7)$$

where I_{max} and I_{min} are the maximum and minimum intensities recorded by the detector across a single fringe. This calculation was performed on a pixel-by-pixel basis for the entire image using the Image Calculator feature of Fiji. Values were then measured across the diagonal of the image perpendicular to the fringes and plotted as a one-dimensional function of x. The function was smoothed over a 4-pixel radius to represent the width of the fringes on the detector.

The SNR of the particles after a phase reconstruction (using a reference hologram) was found by

$$SNR = \pm \frac{|signal - mean_{bg}|}{\sigma_{bg}} \quad (8)$$

Where the $signal$ is the maximum value of the signals peak, $mean_{bg}$ is the mean pixel value of the area surrounding the particle, and σ_{bg} is the standard deviation of the background. For the 8-bit images, the maximum pixel value is 255. Pixel values were obtained of a cross-section of the cell and its surrounding background using Fiji's "plot profile" analysis along a drawn line.

2.2 Sample chamber materials and construction

Sample chambers were constructed by sandwiching a volume of aqueous solution between two of the chosen substrates as in **Figure 2**. Unless stated otherwise, the material used to form the gaskets was adhesive-backed silicone rubber (McMaster-Carr 9010K41), 1/32 of an inch (0.8 mm) thick. Substrates tested were as follows:

Glass slides. (Fisher Scientific).

Polymer. Gas-permeable imaging quality polymer coverslips (ibidi GmbH, Cat #10813).

Pressed polyvinyl chloride ("vinyl"). Unbreakable Cover Slips, Fisherbrand, Fisher Scientific #12-547.

PDMS. The PDMS chamber was a gift of Douglas Weibel, University of Wisconsin-Madison, as described in [46].

Polycarbonate. Polycarbonate sample chamber, 0.18 mm thick polycarbonate with 0.9 mm deep well (Electron Microscopy Sciences 70327-10).

Some substrates were tested with the substrate as both top and bottom, and some with the substrate on the bottom and a glass microscope coverslip as the top layer (coverslip: Fisher Scientific 12-545F), for a total of 7 types of samples: Glass slide/coverslip; polymer/polymer; vinyl/coverslip; vinyl/vinyl; PDMS/coverslip; polycarbonate/coverslip; polymer/polymer.

All sample types were tested with 405 nm illumination; some were additionally tested with 520 nm illumination. At least 2 independently constructed chambers were made of each type to verify consistency.

2.3 Biological samples

Uniform concentrations of the bacteria *Bacillus subtilis* (ATCC 6051, purchased from American Type Culture Collection) or *Vibrio alginolyticus* (YM4, gift of Roman Stocker) were used in the quantification of signal-to-noise ratio. and cultured overnight in appropriate media (lysogeny broth [LB] for *B. subtilis* and Marine Broth 2216 for *V. alginolyticus* [both from Fisher Scientific]). Samples for imaging were 1:100 dilutions of overnight mid-log cultures (OD600~0.8) into fresh medium. Reference channels were filled with sterile medium.

3. Results

3.1 Fringe visibility

In off-axis holography, fringe visibility plays a major role in the image quality obtained after numerical reconstruction [44, 45]. The magnitude of noise in phase images is seen to be inversely and linearly proportional to fringe visibility, as seen in Eqs (2) and (3). By quantifying the fringe visibility of off-axis holograms, a direct inference of phase noise can be established. **Fig. 2A** shows the fringe visibility calculated from Eq. (7) for the microscope with an empty sample path; the line along which visibility was measured is indicated. **Fig. 2B** shows the same calculation for vinyl. **Fig. 2C** shows polymer, and **Fig. 2D** is glass. **Figure 2E** shows a plot of the visibility for all of our sample types with Gaussian fits; **Table 1** gives maximum and minimum values. Fringe visibility is non-uniform across a hologram as light sources have a finite coherence length. This is a property of the laser and so must be considered in choosing a laser; for the Thorlabs diode lasers used here, the coherence envelope was significantly larger for 520 nm than 405 nm illumination (**Fig 2F**).

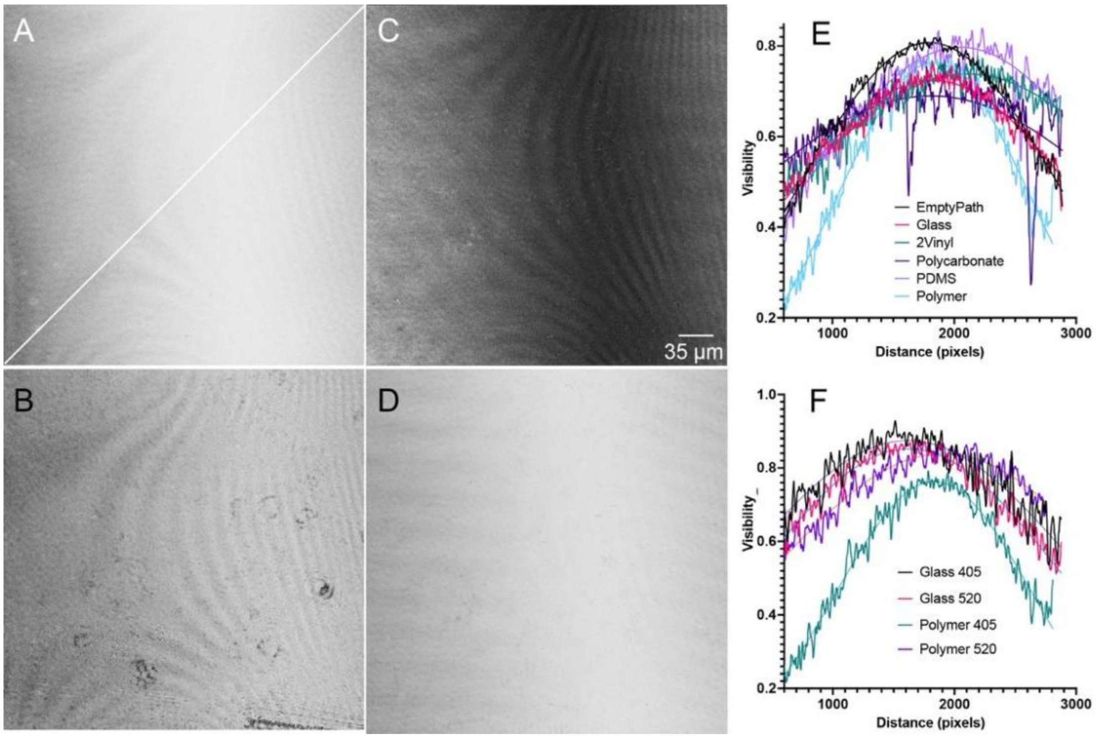

Fig. 2: Fringe visibility. Calculated according to Eq. (7), measured from the bottom left to top right of the hologram. (A) Empty path. (B) Vinyl/vinyl. (C) Polymer/polymer. (D) Glass/Glass. (E) Plot of visibility with Gaussian fits from 600-3000 pixels. (F) Visibility for the polymer substrate with violet (405 nm) vs green (520 nm) illumination.

3.2 Phase noise

Fig. 3 shows a plot of all sample chamber configurations' radially averaged PSD functions, according to Equation 5. The control represents the inherent PSD of the DHM without sample or substrate in the optical path. **Figure 3B** shows the net phase noise of each sample chamber configuration relative to the control value, according to Equation 5.

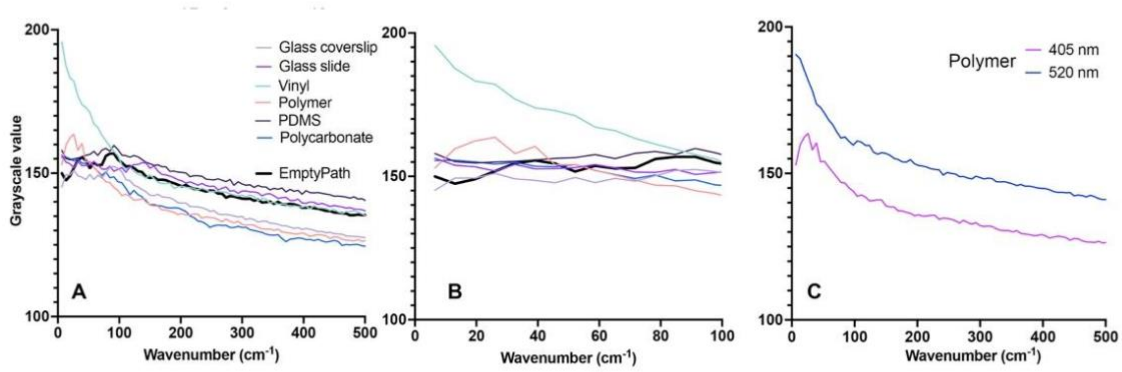

Fig. 3: Phase noise. Shown as radial plot of FFT of raw phase reconstructions on different substrates. (A) 0-500 wavenumbers. (B) Smaller range highlighting areas of low frequency where most variations in substrate occurred. (C) Comparison of a single substrate (polymer) under violet (405 nm) and green (520 nm) illumination.

3.3 Signal to noise of individual bacteria

The practical measure of a substrate's utility is its ability to support detection of the targets. For motile bacteria, or particles with fluid flow, median subtraction of images and/or use of a reference hologram will compensate for optical aberrations. The goal of this section was to determine whether the sample chamber substrates affected the signal to noise of bacteria near the system's resolution limit after optimal aberration compensation was performed in both amplitude and phase. **Fig. 4** shows examples of raw and de-noised amplitude and phase images on two substrate types. **Fig. 4A,B** shows phase images on glass with a reference hologram used for aberration compensation. The full field of view is shown to illustrate the system's optical aberrations; an inset shows a single cell. **Fig. 4C,D** shows corresponding images on polymer substrates. **Fig. 4E** shows a raw amplitude image and **Fig. 4F** an amplitude image denoised by median subtraction of the median image over time at the same focal plane. It can be appreciated that the raw amplitude images are noisier than the phase images, but that median subtraction removes speckle and results in high contrast cell images. **Fig. 4G,H** shows the corresponding raw and median subtracted amplitude images on the polymer substrate.

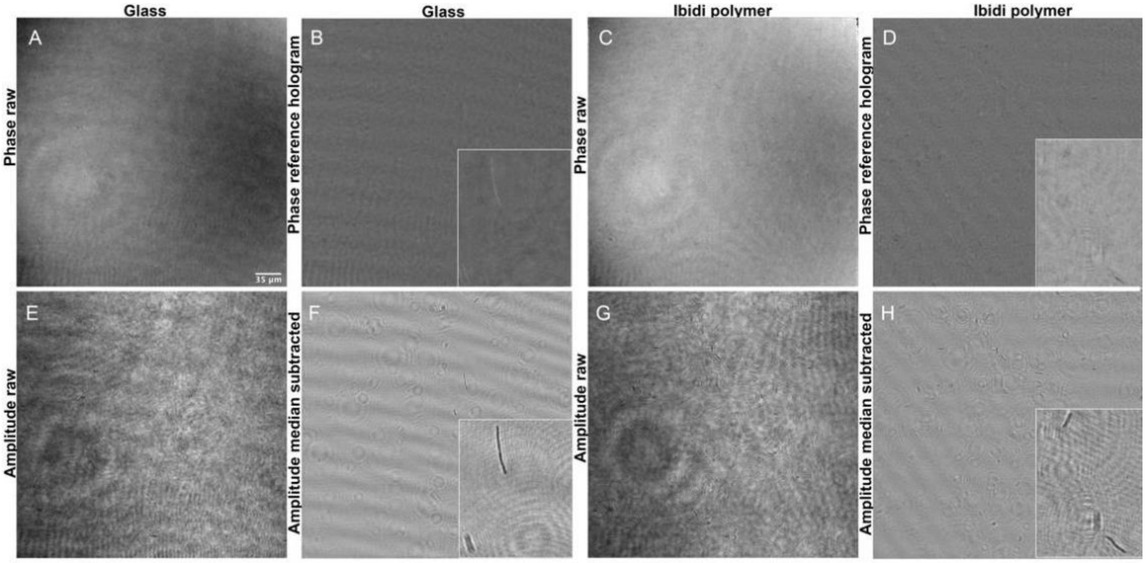

These images were used to evaluate the signal to noise of individual cells on each substrate type in both amplitude and phase. Due to off-axis DHM's ability to conduct volumetric electric field reconstructions, the analysis of volumetric phase images necessitates the consideration of the Gouy phase shift. The Gouy phase shift is the phase advance of a wave as it passes through focus. For spherical waves, this phase advance is exactly π [48-51]. **Fig. 4** shows an axial slice of phase reconstructions through a single cell, illustrating the Gouy phase shift. **Fig. 4** illustrates the Gouy phase shift by plotting the phase value at the center of a single *B. subtilis* bacterium as a function of axial dimension (z). With phase reconstructions bounded between $[-\pi,\pi]$ in addition to the presence of the Gouy phase shift gives rise to both a positive and negative SNR as the phase signal of a bacterium experiences a sign change as it advances by . Both positive and negative SNRs are considered in this work for the phase images.

Table 1. Fringe visibilities of slide/coverslip combinations

	Empty Path	Glass	Glass/ Vinyl	2 Vinyl	Polycarbonate	PDMS	Polymer
Number of values	2888	2878	2771	2871	2890	2854	2809
Minimum	0.1293	0.1848	0.000	0.2761	0.1518	0.1652	0.1108
Maximum	0.8452	0.8143	0.8508	0.8605	0.8245	0.8884	0.8302
Range	0.7158	0.6295	0.8508	0.5843	0.6727	0.7232	0.7194
Mean	0.6005	0.5878	0.6026	0.6212	0.6157	0.6136	0.5038
Std. Deviation	0.1831	0.1268	0.1378	0.1202	0.09885	0.1847	0.1959
Std. Error of Mean	0.003407	0.002364	0.002617	0.002243	0.001839	0.003458	0.003696

Figure 5 shows the calculated mean values for particles viewed through the different substrates. Twelve particles were examined in each recording, six at either end of the Guoy phase shift. A mean was taken at each point in the data, to obtain a dataset that is the mean of the particles. Cells selected for examination were chosen using the criteria that they were in focus at specific z-planes and were not in the same line as other cells. Some cells were impacted by debris or surface imperfections, as discussed later.

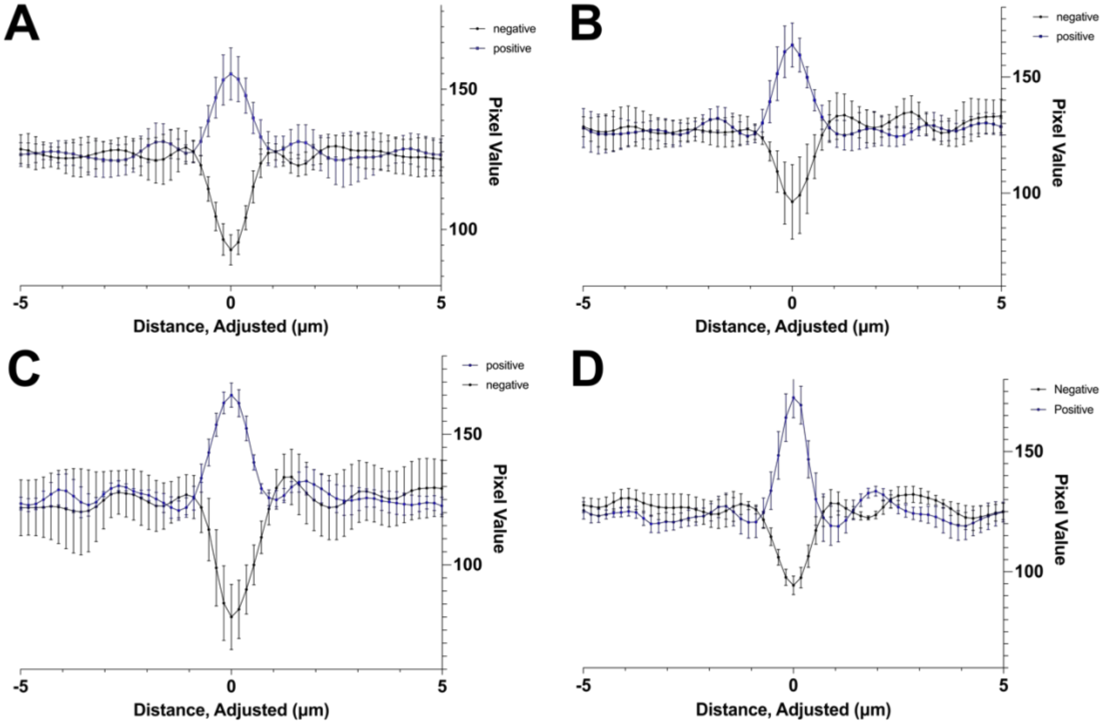

Figure 5: The plot profile of the average of the individual signals in a recording. Signal peaks were aligned and then point-by-point averages taken. Standard deviation for each mean was also calculated and is shown. The particles were separated by positive or negative before averaging. A) Mean plot profile through two glass microscope slides. B) Mean plot profile through one vinyl coverslip and one glass coverslip. C) Mean plot profile through two vinyl coverslips. D) Mean plot profile through one polycarbonate and one glass coverslip.

The SNR of the examined particles was calculated as per **Equation 8**. The mean SNR was calculated for both the positive and negative SNR values. Average SNR for both the positive and negative cases are shown below in **Figure 6**.

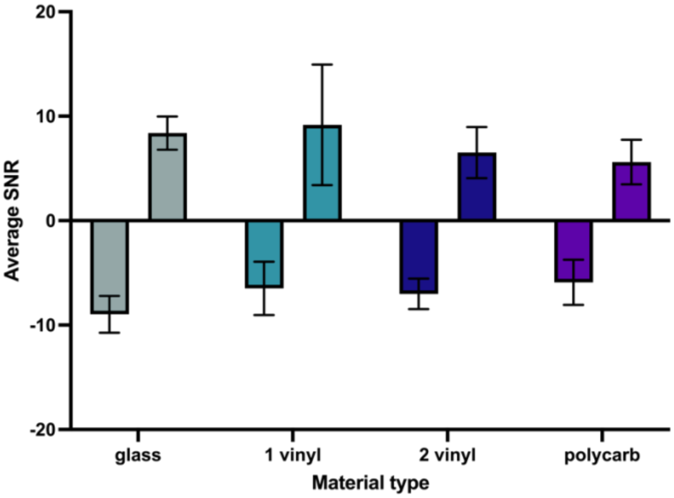

Figure 6: SNR comparison. Mean SNR for the negative and positive values for the glass, glass/vinyl, vinyl/vinyl, and polycarbonate/glass sample chambers.

4 Discussion

Each of the described substrates was sufficient for use in DHM, but features of certain materials impact use. The vinyl coverslips, while unbreakable and showing a mean SNR (for the 'negative' side of the Guoy phase shift) comparable to other substrates, have high variation in surface quality due to debris and scratches. Vinyl coverslips required cleaning in a sonic bath with standard dish soap to remove debris followed by a rinse in 70% EtOH to remove leftover debris. They were then rinsed in 100% EtOH to remove soap residue and dried water droplets. Harsher surface treatments, such as Piranha, damaged the coverslips and could not be used. This process helped remove debris stuck to the surface, but remaining particles were visible under the DHM. In addition, the coverslips were found to have abrasions 10s of microns wide and up to 100s of microns long. These impacted cell visibility in those regions and would likely make tracking cell movement in these regions difficult.

Preliminary comparison of SNR and qualitative analysis of cell visibility was done to investigate the role of light source wavelength in DHM. In initial testing, *Vibrio alginolyticus* in chambers made of vinyl coverslips were examined under 405nm, 520nm, and 635nm single-wavelength light sources (Thorlabs). By human inspection, cells were most easily visible under the 520nm light—when using red light, the small size of *V. alginolyticus* was unable to be resolved. Cells were also well-defined under 405nm light, but the shorter wavelength emphasized the imperfections in the vinyl coverslips, effecting cell visibility. Further testing is required to quantify this effect and is beyond the scope of the work documented here. The features of the substrate, such as those described in the vinyl coverslips, made establishing the focal plane challenging—particularly for systems with and adjustable focus system.

The work included in this study also serves as preliminary testing for development of custom sample chambers for motility studies. In this continuing work, the ability to adhere the substrates to other materials is an important consideration. Additional testing is necessary to examine other properties that influence motility studies—such as gas permeability through the substrates and impacts on cell survivability.

Funding

National Science Foundation (1828793). Portions of this work were supported under a contract from, or performed at, the Jet Propulsion Laboratory, California Institute of Technology, under a contract with the National Aeronautics and Space Administration.

Acknowledgments

Disclosures. The authors declare no conflicts of interest.

Data availability

The raw holograms for the datasets used here are deposited in a public depository at Data Dryad, contact authors for access. Other data, such as reconstructions, are available from the authors upon request. The software packages used are all open source and are available at the following sites: acquisition software, DHMx: https://github.com/dhm-org/dhm_suite; Reconstruction Fiji plug-ins: https://github.com/sudgy/.

References

1. J. L. Nadeau, Y. B. Cho, and C. A. Lindensmith, Optics letters **40**, 4114 (2015).
2. W. Denk, J. Strickler, and W. Webb, Science (New York, N.Y.) **248**, 73 (1990).
3. C. R. Burch, and J. P. P. Stock, Journal of Scientific Instruments **19**, 71 (1942).
4. F. Zernike, Monthly Notices of the Royal Astronomical Society **94**, 377 (1934).
5. T. E. Gureyev, and K. A. Nugent, Optics Communications **133**, 339 (1997).
6. N. Lue, W. Choi, G. Popescu, T. Ikeda, R. R. Dasari, K. Badizadegan, and M. S. Feld, Applied Optics **46**, 1836 (2007).
7. E. Cuche, F. Bevilacqua, and C. Depeursinge, Optics Letters **24**, 291 (1999).
8. U. Schnars, and W. P. Jüptner, Measurement science and technology **13**, R85 (2002).
9. T. Ikeda, G. Popescu, R. R. Dasari, and M. S. Feld, Optics Letters **30**, 1165 (2005).
10. G. Dunn, and D. Zicha, "Using DRIMAPS system of transmission interference microscopy to study cell behavior," (San Diego: Academic press, 1998).
11. D. J. Stephens, and V. J. Allan, Science (New York, N.Y.) **300**, 82 (2003).
12. C. Dunsby, Optics Express **16**, 20306 (2008).
13. S. Kumar, D. Wilding, M. B. Sikkel, A. R. Lyon, K. T. MacLeod, and C. Dunsby, Optics Express **19**, 13839 (2011).
14. K. K. KyeoReh Lee, Jaehwang Jung, JiHan Heo, Sangyeon Cho, Sangyun Lee, Gyuyoung Chang, YoungJu Jo, Hyunjoo Park, YongKeun Park, Sensors **13**, 21 (2013).
15. F. Dubois, C. Yourassowsky, O. Monnom, J. C. Legros, O. Debeir, P. Van Ham, R. Kiss, and C. Decaestecker, J Biomed Opt **11**, 054032 (2006).
16. M. Falck Miniotis, A. Mukwaya, and A. Gjorloff Wingren, PLoS One **9**, e106546 (2014).

17. P. Jourdain, N. Pavillon, C. Moratal, D. Boss, B. Rappaz, C. Depeursinge, P. Marquet, and P. J. Magistretti, J Neurosci **31**, 11846 (2011).

18. B. Kemper, D. Carl, J. Schnekenburger, I. Bredebusch, M. Schafer, W. Domschke, and G. von Bally, J Biomed Opt **11**, 34005 (2006).

19. N. Pavillon, J. Kuhn, C. Moratal, P. Jourdain, C. Depeursinge, P. J. Magistretti, and P. Marquet, PLoS One **7**, e30912 (2012).

20. B. Rappaz, B. Breton, E. Shaffer, and G. Turcatti, Comb Chem High Throughput Screen **17**, 80 (2014).

21. B. Rappaz, P. Marquet, E. Cuche, Y. Emery, C. Depeursinge, and P. Magistretti, Opt Express **13**, 9361 (2005).

22. T. Ahmed, T. S. Shimizu, and R. Stocker, Nano letters **10**, 3379 (2010).

23. C. Giuffre, P. Hinow, R. Vogel, T. Ahmed, R. Stocker, T. R. Consi, and J. R. Strickler, PloS one **6** (2011).

24. M. Molaei, M. Barry, R. Stocker, and J. Sheng, Physical review letters **113**, 068103 (2014).

25. T. Colomb, J. Kuhn, F. Charriere, C. Depeursinge, P. Marquet, and N. Aspert, Opt Express **14**, 4300 (2006).

26. H. Wang, M. Yu, Y. Jiang, Q. Zhu, and F. Liu, Optics Communications **322**, 90 (2014).

27. Z. Wang, W. Qu, Y. Wen, F. Yang, and A. Asundi, International Conference on Experimental Mechanics 2014 **9302** (2015).

28. F. Pan, W. Xiao, S. Liu, F. Wang, L. Rong, and R. Li, Optics Express **19**, 3862 (2011).

29. B. Le Thanh, M. Piao, J.-R. Jeong, S.-H. Jeon, and N. Kim, Journal of the Optical Society of Korea **19**, 22 (2015).

30. X. J. Lai Xin-Ji, H.-Y. Tu, C.-H. Wu, Y.-C. Lin, and C.-J. Cheng, Applied Optics **54**, 51 (2015).

31. M. Matrecano, P. Memmolo, L. Miccio, A. Persano, F. Quaranta, P. Siciliano, and P. Ferraro, Applied Optics **54**, 3428 (2015).

32. A. Sharma, G. Sheoran, and Z. Jaffery, Optics and lasers in engineering **46**, 42 (2008).

33. E. Cuche, P. Marquet, and C. Depeursinge, Applied Optics **39**, 4070 (2000).

34. P. Memmolo, V. Bianco, M. Paturzo, B. Javidi, P. A. Netti, and P. Ferraro, Optics Express **22**, 25768 (2014).

35. M. Molaei Mehdi, and J. Sheng, Optics Express **22**, 32119 (2014).

36. F. Charrière, T. Colomb, F. Montfort, E. Cuche, P. Marquet, and C. Depeursinge, Applied Optics **45**, 7667 (2006).

37. N. Demoli, H. Skenderovic, and M. Stipcevic, Optics Letters **39**, 5010 (2014).

38. D. G. Sirico, L. Miccio, Z. Wang, P. Memmolo, W. Xiao, L. Che, L. Xin, F. Pan, and P. Ferraro, Applied Physics B **128**, 78 (2022).

39. J. K. Wallace, S. Rider, E. Serabyn, J. Kuhn, K. Liewer, J. Deming, G. Showalter, C. Lindensmith, and J. Nadeau, Opt Express **23**, 17367 (2015).

40. J. Schindelin, I. Arganda-Carreras, E. Frise, V. Kaynig, M. Longair, T. Pietzsch, S. Preibisch, C. Rueden, S. Saalfeld, B. Schmid, J. Y. Tinevez, D. J. White, V. Hartenstein, K. Eliceiri, P. Tomancak, and A. Cardona, Nature methods **9**, 676 (2012).

41. D. Cohoe, I. Hanczarek, J. K. Wallace, and J. Nadeau, Frontiers in Physics **7** (2019).

42. C. Mann, L. Yu, C. M. Lo, and M. Kim, Opt Express **13**, 8693 (2005).

43. T. Colomb, E. Cuche, F. Charriere, J. Kuhn, N. Aspert, F. Montfort, P. Marquet, and C. Depeursinge, Appl Opt **45**, 851 (2006).

44. D. C. Champeney, *Fourier Transforms and Thier Physical Applications* (Academic Press, Inc. (London) LTD., 1973).

45. M. C. A. Sumner P. Davis, James W. Brault, *Fourier Transform Spectroscopy* (Academic Press, 2001).

46. J. A. Crooks, M. D. Stilwell, P. M. Oliver, Z. Zhong, and D. B. Weibel, Chembiochem **16**, 2151 (2015).

47. M. Bedrossian, J. Nadeau, E. Serabyn, and C. Lindensmith, "Sources and propagation of errors in quantitative phase imaging techniques using optical interferometry," in *Quantitative Phase Imaging III*(International Society for Optics and Photonics2017), p. 100740E.

48. L. G. Gouy, CR Acad. Sci. Paris **110**, 1251 (1890).

49. T. D. Visser, and E. Wolf, Optics Communications **283**, 3371 (2010).

50. S. Feng, and H. G. Winful, Optics Letters **26**, 485 (2001).

51. L. G. Gouy, Compt. Rendue Acad. Sci. Paris **111**, 33 (1890).

Concluding Chapter

The work in this document improved the ability to study microbes in conditions beyond those found in the laboratory. Continuing work, based on results described here, is underway. This includes, but is not limited to: development and NASA qualification testing for the systems launching to the ISS, examination of other species of micro-organisms using the heated bath system (including the thermophilic archaea *Pyrococcus furiosus*), and analysis of field samples collected from the crater of Mt. St. Helen's in September 2021. It is worth noting that Chapters 2 and 4 reflect the draft of articles being submitted for publication, but the version published in the journals is subject to change by the time of publication of this work.

One goal of the publication of these works is to showcase affordable but reliable systems for studying motility in the hopes that others will utilize them. It is the authors hope that others will construct these heated bath systems to expand the understanding of organisms that thrive in environments not suited to the standard laboratory setting. The heated bath system has since been tested for its ability to be traveled with and use for field samples.

In addition, the authors (and others who continue development of the system for the ISS) hope that publication of the materials in Chapter 4 and future publications on flight-certified sample chambers will encourage more detailed discussion about the chambers being used in the field and lead to increased standardization in design and quality. After certification and completed testing, details and models of finished designs will be made public access.